Genetically encoded self-assembling synuclein for tunable Parkinsonian pathology *in vitro* and *in vivo*

Yujie Fan[1,2], Jonathan D. Hoang[1,2], Chelsie Steele[1], Yochana Benchetrit[1], Sayan Dutta[1,2], Gerard M. Coughlin[1,2], Nathan Appling[1], Xiaozhe Ding[1], Changfan Lin[1], Zhe Qu[1], Viviana Gradinaru[1,2,*]

[1] Division of Biology and Biological Engineering, Caltech, Pasadena, CA 91125
[2] Aligning Science Across Parkinson's (ASAP) Collaborative Research Network, Chevy Chase, MD 2081

*Correspondence to: viviana@caltech.edu

Abstract

Many neurodegenerative diseases feature abnormal protein aggregation in neurons. A notable example is α-synuclein (αSyn) aggregates in Parkinson's disease (PD). The mechanisms underlying aggregates formation and their contribution to the pathogenesis remain unclear. Here we tackle this question from a build-to-understand perspective by recreating αSyn aggregates that recapitulate PD pathologies. We developed a novel system, named self-assembling α-synuclein (SAS), which enables αSyn to form different types of aggregates intracellularly. By screening various SAS constructs, we identified those that induce key PD pathologies, including Ser129 phosphorylation of αSyn (pS129-αSyn) and neurite retraction. As a genetically-encoded system, SAS can be seamlessly applied to a wide range of *in vitro* and *in vivo* models. *In vitro*, SAS led to strong pS129-αSyn, secondary aggregation of endogenous αSyn, mitochondrial deficits and neuronal degeneration in primary neurons, hESC-derived neurons and organoids. To further validate if SAS-induced aggregates recapitulate PD pathologies *in vivo*, we systemically delivered SAS into mouse brain using the adeno-associated virus PHP.eB. SAS-injected mice exhibited impaired motor function, dopaminergic neuron loss and reduced striatal projections. Furthermore, dopaminergic neuron-targeted SAS recapitulated motor deficits and revealed that induced αSyn aggregates can propagate from substantia nigra to other brain regions. This study establishes SAS as a robust and widely applicable system for temporally-controllable, tunable, and cell-type-specific PD pathology. By closely mirroring human PD pathology in terms of histology hallmarks, transcriptional profiles, and behavioral outcomes, SAS provides a powerful tool to investigate disease mechanisms and therapeutic interventions, with potential applicability to other neurodegenerative diseases.

Keywords

Parkinson's disease; Self-assembling protein; Alpha-synuclein; Preclinical models; Protein engineering; Neurodegenerative diseases.

Main

A defining feature of many neurodegenerative diseases is abnormal protein misfolding and aggregation[1]. Although different diseases involve distinct protein aggregates in different brain regions, they share many commonalities. Abnormal protein aggregation causes mitochondria dysfunction, synaptic deficits, and inflammatory responses, eventually leading to neuronal loss and behavioral changes[1,2]. Protein aggregates can spread from one neuron to another in a prion-like manner, propagating pathology across neural circuits[2,3]. It remains largely unknown what triggers protein misfolding, which forms of aggregates are toxic, how do aggregates spread between cells, and why are certain neurons and brain regions more vulnerable than others. Furthermore, protein misfolding and aggregation may begin decades before clinical symptoms[4]. Capturing this slow progression is difficult, making it extremely challenging to model and study neurodegenerative diseases in experimental models.

Parkinson's disease (PD) is characterized by the progressive loss of dopaminergic (DA) neurons in the substantia nigra pars compacta (SNpc) and the formation of intracellular inclusions known as Lewy bodies (LBs) and Lewy neurites (LNs)[5–7]. The main component of LBs and LNs is aggregates of misfolded α-synuclein (αSyn). It remains unclear when, where, and in which cell types αSyn aggregation starts, how the aggregates propagate between cells, and why the DA neurons in the SNpc are more vulnerable to degeneration[8,9]. Over the past two decades, numerous *in vitro* and *in vivo* models have been developed for PD, each offering unique insights into disease mechanisms[10–12]. Toxin-based models, such as 6-hydroxydopamine (6-OHDA), induce rapid DA neuron degeneration but typically fail to produce LBs and LNs pathology[13,14]. Genetic models involving PD-related mutations, including the gene encoding αSyn (*SNCA*), replicate the genetic background of familial PD but often do not exhibit key pathological hallmarks such as nigrostriatal degeneration, motor deficits, and αSyn inclusions[15]. The αSyn pre-formed fibril (PFF) model has recently gained prominence, with intracerebral injection of αSyn PFFs in rodents inducing neurodegeneration and behavioral deficits[16–18]. Despite its promise, this model requires invasive surgical procedures and lacks cell-type specificity. Additionally, in stem cell-derived neurons and organoids, the PFF model is further limited by low cellular uptake and poor penetration into deeper layers of 3D organoids.

To address these challenges, we developed a self-assembling αSyn (SAS) system that generates intracellular αSyn aggregates, enabling temporally-controlled, tunable, and cell-type-specific modeling of PD pathology. This platform allows rapid screening of self-assembling variants to identify those best recapitulating PD pathology. We identified SAS constructs forming proteinase K-resistant aggregates that induced significant Ser129 phosphorylation of αSyn (pS129-αSyn), secondary αSyn aggregation, and neurite retraction. Non-invasive delivery of SAS into the mouse brain resulted in impaired motor function, DA neuron loss in the SNpc, and diminished projections to the striatum. Delivering SAS specifically to DA neurons demonstrated that SNpc neurons were more vulnerable to degeneration than those in the ventral tegmental area and that αSyn aggregates

can propagate from the SNpc to other brain regions. The transcriptomic analysis further revealed that SAS expression promoted inflammatory responses, mitochondrial damage, and neuronal death. In this study, we present the novel SAS system for inducing tunable PD pathology in diverse experimental models, closely mirroring human PD pathology in terms of histology hallmarks, transcriptional profiles, and behavioral outcomes.

Results

Self-assembling synuclein (SAS) drives tunable synucleinopathy

LBs consist mainly of misfolded αSyn, along with other cellular components[19]. Instead of synthesizing pure αSyn aggregates in solution and then introducing them into cells, we hypothesized that inducing αSyn aggregation intracellularly would enable the aggregates to incorporate endogenous cellular components, therefore more faithfully recapitulating synuclein-related pathologies. De novo-designed helical filaments[20,21] and naturally existing self-assembling proteins[22,23] have been shown to aggregate spontaneously in solution or in yeast. Additionally, self-assembling proteins have been applied to record protein activity *in vivo*[24,25]. Inspired by these studies, we designed a library of self-assembling synuclein (SAS), each consisting of αSyn fused with a different self-assembling protein (SAP) at a position that remains accessible on the exterior surface of the resulting filament (**Table S1**). To achieve precise control over expression level and timing, we integrated this design into a doxycycline-regulated system. Cell-type specificity is facilitated by utilizing cell-type-specific promoters to drive expression of the reverse tetracycline-controlled transactivator (rtTA), allowing for targeted induction of α-synuclein aggregation in desired cell populations (**Fig. 1a**).

In vitro screening in HEK cells identified several constructs that not only form αSyn aggregates but also induce substantial Ser129 phosphorylation of αSyn (pS129-αSyn), a hallmark of αSyn pathology (**Fig. 1b and S1a**). Different SASs resulted in different types of aggregates with various abilities to induce pS129-αSyn. For example, SAS3 formed condensed punctate structures and robustly induced pS129-αSyn. To confirm that the pS129-αSyn induction was specific to the αSyn aggregates, we compared SAS3 with rtTA-transfected control (ctrl), *SNCA* overexpression (OE) and SAP alone. Only SAS3 led to strong pS129 induction; αSyn OE or SAP alone did not trigger this strong pathology (**Fig. 1b**). Western blot analysis confirmed that SAS3 induced more than 1000-fold higher pS129-αSyn compared to αSyn OE (**Fig. 1c&d and S1b&c**), underscoring its potential to recapitulate PD pathology.

The SAS system allows precise control of αSyn aggregation and pathology through manipulation of doxycycline (dox) concentration and treatment duration. Titration of dox concentration decreased the average number and size of aggregates (**Fig. 1e, f, and g**), shifting the aggregate size distribution (**Fig. S1d**). Prolonged dox treatment led to a corresponding growth in aggregate size and increase of αSyn phosphorylation (**Fig. S1e**). The tunability of the SAS system allows

researchers to quantitatively model PD pathology with varying severity, providing a robust, scalable, and tunable preclinical model for studying disease mechanisms and developing therapeutics.

SAS induces neurite retraction and endogenous αSyn aggregation

Another hallmark pathology of PD is neuronal degeneration. After demonstrating that SAS induces strong αSyn aggregation with pS129-αSyn in HEK cells, we next investigated whether SAS could induce similar pathology in neurons and, most importantly, whether the SAS-mediated synucleinopathy leads to neuronal degeneration. The SAS system was delivered to the mouse primary neurons using adeno-associated virus (AAV) AAV9-X1.1[26], an engineered AAV that can efficiently transduce primary murine and human neurons in culture[27] (**Fig. 2a**). As observed in HEK cells, SAS3 induced robust αSyn aggregation and pS129-αSyn in both the soma and neurites of primary neurons (**Fig. 2b)** and quantified in **Fig. 2c&d and S2a**. Beyond aggregation, SAS3-transduced neurons exhibited pronounced neurite retraction after 3 days of dox treatment (**Fig. 2b&e**), mimicking the neurodegenerative feature in PD. Consistent with these findings, SAS3 also induced αSyn aggregation and neurite retraction in human embryonic stem cell (hESC)-derived neurons (**Fig. S2b**).

PD is considered a prion-like disease. Abnormal αSyn aggregates can induce secondary nucleation of normal αSyn[28–30], promoting disease spreading. To determine whether SAS-induced aggregates possess this capability, we used primary neurons that expressed an SNCA-GFP reporter, enabling tracking of the endogenous αSyn. Following 36 hours of dox treatment, neurons expressing SAS3 exhibited degeneration phenotypes compared with control groups (**Fig. 2g**), with further worsening by 72 hours (**Fig. S2c**). Close examination of SAS3-transduced neurons revealed endogenous αSyn aggregation in both soma and neurites (**Fig. 2h**), suggesting a prion-like seeding effect.

Collectively, these results demonstrated that SAS induced both primary and secondary αSyn aggregation, leading to significant neuronal degeneration. The ability of SAS to induce these key PD pathological features highlights its potential as a valuable model for studying αSyn-driven neurodegeneration and PD progression.

SAS-induced-aggregates colocalize with mitochondria, and drive neuronal death and inflammation

Postmortem examination of PD patients has shown aggregates are far from homogeneous lumps of toxic protein[31]. LBs often contain hundreds of different proteins and even entire membranous organelles tangled up in them[32,33]. One significant advantage of the SAS system is its intracellular formation of the aggregates, allowing for the incorporation of other cellular components. hESC-derived organoids produce diverse cell types in a 3D environment that closely mimics the function and structure of *in vivo* counterparts. We utilized hESC-derived organoids to investigate if SAS-induced aggregates could trap other cellular components like LBs (**Fig. 3a**). Previous organoid-

based PD models failed to display hallmark features of PD, such as LBs formation and neuronal degeneration. For example, αSyn PFFs, which have shown promise in animal studies, do not work in organoids due to poor uptake and penetration (**Fig. 3b**). The genetically-encoded and AAV-delivered SAS3 was able to efficiently access organoids (**Fig. 3b and S3a&b**). Immunostaining for the V5 tag and pS129-αSyn revealed widespread synucleinopathy, with aggregates present even in deep-layer organoids. LBs are known to sequester various cellular components, including mitochondria. To assess whether SAS-induced aggregates contain mitochondria, we performed Z-scanning confocal imaging of organoids stained with the V5 tag to trace aggregates and the mitochondrial marker Tomm20. SAS3-induced aggregates were found to contain mitochondria (**Fig. 3c**), a feature absent in all other control groups (**Fig. S3c**), further supporting their resemblance to LBs.

To profile transcriptional changes in response to SAS-induced aggregates, we conducted bulk RNAseq of SAS-transduced and control organoids. SAS-expressing organoids displayed a distinct transcriptomic profile (**Fig. 3d**), with 178 differentially expressed genes (DEGs) with adjusted p-value < 0.05 and log2 fold change (FC) >1 (**Fig. S3d** and **Table S2**). Pathway analysis revealed significant upregulation of p53 and TNFα signaling, key regulators of apoptosis and inflammation (**Fig. 3e**). Notably, the TNF-NF-κB-p53 axis has been demonstrated to mediate dopamine neuron survival in neuron transplant experiments[34]. Targeting this pathway might enhance neuron survival in PD. Consistent with human transcriptomic data[35], SAS-treated organoids showed activation of apoptosis, inflammation, and mitochondrial dysfunction pathways (**Fig. 3f and S3e**). Among the top 25 most dysregulated genes, many were previously implicated in PD (**Fig. 3g)**. For example, *FDXR*, which encodes the mitochondrial ferredoxin reductase that helps produce iron-sulfur clusters, has been implicated in neurodegeneration associated with inflammation[36].

These findings demonstrate, for the first time, that key PD pathologies—including αSyn aggregation, neuronal degeneration, incorporation of cellular organelles, and disease-associated transcriptomic changes—can be fully recapitulated in human brain organoids. This breakthrough opens new avenues for patient-derived induced pluripotent stem cell (iPSC)-based studies to investigate the role of genetic mutations, conduct large-scale drug screening, develop diagnostic biomarkers and more.

SAS induces PD-relevant histopathology and behavioral deficits in mice

The primary clinical manifestation of PD is movement disorder. To investigate whether SAS can induce behavior abnormalities in mice, we utilized AAV-PHP.eB, a capsid capable of crossing the blood-brain barrier (BBB), to achieve non-invasive delivery of SAS into the mouse central nervous system (CNS)[37]. To specifically target neurons, we used the human synapsin (hSyn) promoter to drive the expression of rtTA. The hSyn-rtTA and TRE-SAS3 constructs were packaged into AAV-PHP.eB and co-delivered into wild-type (WT) C57BL/6J mice via retro-orbital (RO) injection. Dox treatment started 2 weeks after virus injection and behavioral assays were performed every

other week (**Fig. 4a**). After 4 weeks of dox treatment, SAS3-treated mice exhibited a progressive decline in movement in the open field test (OFT) compared to control groups (**Fig. 4b**). Additionally, these mice demonstrated an increased gut transit time following 4 weeks of dox treatment, although this phenotype diminished by 8 weeks (**Fig. 4c**). Mice were sacrificed at week 8 for histological analysis to assess neuropathological changes associated with SAS3 treatment. We first examined the olfactory bulb (OB), where PHP.eB strongly transduced. Consistent with our *in vitro* findings, SAS-induced aggregates were associated with robust pS129-αSyn staining, whereas the control (hSyn-rtTA only), *SNCA* OE, and SAP did not show significant pS129-αSyn signal (**Fig. 4d and S4a**). Next, we examined other brain regions and found SAS-induced aggregates in the cortex, hippocampus (**Fig. S4b**) and substantia nigra (**Fig. 4e**). Strikingly, the SNpc exhibited a clear reduction in TH+ neurons (**Fig. 4e**), and the intensity of DA neuron projections was significantly diminished in the striatum (**Fig. 4f&g**). Finally, proteinase K treatment of the SAS3-transduced brain confirmed the resistance of the aggregates to proteolytic degradation (**Fig. S4c**), further supporting their pathological relevance.

SAS activates microglia and triggers immune response in mice

To dissect transcriptional changes in response to SAS-induced aggregates *in vivo*, we performed bulk RNAseq of the OB, a region strongly transduced by PHP.eB. SAS-transduced mice displayed a distinct transcriptome compared with control mice expressing only rtTA (**Fig. 5a**). Differential gene expression analysis identified 139 DEGs with adjusted p-values < 0.05 and log2FC >1 (**Table S3**), with a strong enrichment of genes promoting inflammation (**Fig. 5b**). Pathway analysis confirmed robust activation of inflammatory and immune responses (**Fig. 5c & S5a**). Among the top 25 most dysregulated genes (**Fig. 5d**), several key inflammatory pathways were highly upregulated, including the interferon-gamma (IFN-γ), tumor necrosis factor-alpha (TNF-α), toll-like receptor (TLR), and interleukin (IL) signaling (**Fig. 5e**).

We also observed a significant upregulation of genes associated with microglial activation in SAS-transduced mice (**Fig. 5f**). For example, IBA1, encoded by the *Aif1* gene, was markedly increased in SAS3-treated mice. CXCL9, a chemokine produced by microglia that plays a crucial role in neuroimmune responses, exhibited an approximately 500-fold upregulation. CST7, a cystatin that has been implicated in microglial activation under disease conditions and is linked to pathways involved in phagocytosis, cytokine/chemokine signaling, and antigen presentation, was also highly expressed. Additionally, complement protein C3, a key activator of microglia, showed a 60-fold increase. These changes strongly indicate a pronounced microglial activation state in SAS3-treated mice. Immunostaining of astrocytes (GFAP) and microglia (IBA1) confirmed that activated microglia clustered around SAS-induced aggregates, suggesting a targeted immune response to pathological protein accumulation (**Fig. 5g and S5b**). Collectively, these findings highlight the profound neuroinflammatory impact of SAS-induced aggregates, mirroring key aspects of PD pathology.

Dopaminergic neuron-targeted SAS recapitulates motor deficits and PD histopathology

As a genetically encoded system, SAS provides a well-defined platform to dissect the roles of specific cell types in PD pathology. Degeneration of DA neurons in SNpc causes motor symptoms in PD[38]. To selectively deliver SAS3 into DA neurons, we injected Cre-dependent SAS3 (DIO-SAS3) into TH-Cre mice using AAV-PHP.eB (**Fig. 6a**). 4 weeks post virus injection, SAS3-treated mice started to exhibit significant motor impairments in the beam-crossing assay, requiring more time to traverse the beam (**Fig. 6b**) and displaying an increased number of slips (**Fig. 6c**) compared to control mice. The motor deficits progressively worsened with prolonged dox treatment, indicating ongoing neurodegeneration. Mice were sacrificed at 4, 8 and 12 weeks for histological analysis to assess the progression of pathology. We first examined DA neurons in the SN, the primary target (**Fig. 6d & S6a**). At week 4, SAS-induced aggregates were primarily detected in DA neurons within the ventral tegmental area (VTA) and SNpc. By week 8, the number of aggregates had increased, and many TH+ neurons in the SNpc exhibited a clear reduction in TH expression (**Fig. S6a**). At week 12, while most neurons with aggregates in the VTA retained TH expression (**Fig. 6d, area 1**), a significant proportion of neurons in the SNpc with aggregates exhibited markedly reduced or absent TH expression (**Fig. 6d, area 2**). We also detected SAS-induced aggregates in regions that are not typically targeted by TH-Cre, suggesting potential propagation of aggregates beyond DA neurons (**Fig. 6d, area 3**). A similar trend was observed in the striatum, the primary target of DA neurons from the SNpc. At week 4, no detectable aggregates were present in the striatum (**Figure S6b**). However, aggregates emerged by week 8 (**Fig. S6b**) and became more prominent by week 12 (**Fig. 6e**), suggesting progressive aggregate accumulation and potential spreading along the nigrostriatal pathway. The intensity of TH staining in the striatum also decreased with time (**Fig. 6e & S6b**), reflecting a reduction in dopaminergic innervation, consistent with the observed neurodegeneration in the SNpc. Immunostaining for V5 and pS129-αSyn revealed that not only were SAS-induced aggregates strongly phosphorylated (**Fig. 6f, arrows**), but a significant amount of endogenous α-synuclein also aggregated and became phosphorylated (**Fig. 6f, arrowheads**). This again confirmed that SAS3 can induce secondary nucleation of αSyn, contributing to the spread of disease.

Discussion

In this study, we present the development of a self-assembling α-synuclein (SAS) system, which enables intracellular aggregation of αSyn in a temporally controlled, tunable, and cell-type-specific manner. *In vitro*, SAS-induced aggregates led to strong pS129-αSyn, secondary αSyn aggregation and neuronal degeneration in primary neurons, hESC-derived neurons and organoids, capturing key aspects of PD pathology. *In vivo*, non-invasive delivery of SAS into the mouse brain using AAV-PHP.eB resulted in impaired motor function, dopaminergic neuron loss, and inflammation, closely resembling hallmarks of PD progression. Transcriptomic analysis revealed upregulation of inflammatory and apoptotic pathways in SAS-treated human organoids and mice, suggesting

immune activation, as in PD. In summary, we demonstrated that the SAS system offers a valuable tool to model and study PD, which can be seamlessly applied to diverse experimental models.

When screening our library of SAS constructs for aggregates that induce pS129-αSyn, we discovered that different types of αSyn aggregates exhibit varying capacities to induce pS129-αSyn. This variation raises intriguing questions about what determines the toxicity of αSyn aggregates. Our findings suggest that high local concentration and structural form of αSyn plays a critical role in toxicity, as SAS3-induced aggregates exhibit significantly higher toxicity than *SNCA* OE despite a lower total amount of αSyn (**Fig. 1c and S1b**). Similar observations have been made comparing αSyn PFFs and αSyn monomers. Furthermore, structure differences appear to influence pathological outcomes, as different SAS constructs induce different levels of toxicity and phosphorylation (**Fig. S1a**). This aligns with studies showing that patient-derived αSyn PFFs exhibit different structural properties and varying neurotoxicity[39]. These observations imply that the structural conformation of αSyn aggregates may be a key determinant of disease progression and severity. Understanding how distinct structural features of α-synuclein aggregates correlate with specific pathological outcomes could provide critical insights into PD pathology.

A key advantage of SAS is its broad applicability across *in vitro* and *in vivo* models, including cell lines (**Fig. 1**), primary neurons (**Fig. 2**), hESC or iPSC-derived neurons, organoids (**Fig. 3**), and mice (**Fig. 4-6**). Notably, SAS demonstrates exceptional performance in hESC-derived neurons and organoids, recapitulating key PD pathological hallmarks, such as Ser129 phosphorylation, neuronal degeneration, and αSyn propagation, a milestone that previous models have struggled to achieve. By leveraging the diverse genetic backgrounds of PD patient-derived iPSCs, along with the scalability and tunability of the SAS system, we are presented with unprecedented opportunities to dissect the roles and mechanisms of genetic and environmental factors in PD progression and to conduct large-scale drug screening to identify potential therapeutic strategies for halting PD progression.

We have shown directly in primary neurons that SAS induces secondary nucleation of endogenous αSyn (**Fig. 2g&h**). This finding is further supported by the presence of V5-negative, pS129-positive aggregates in neurons in multiple, *in vitro* and *in vivo*, systems (**Fig. 2b**, **S2b; Fig. S3a&b; Fig. S6f**). Secondary nucleation is a critical driver of αSyn aggregation spread and amplification, yet its underlying mechanisms remain unclear. Future studies are needed to dissect how primary nucleation triggers secondary nucleation and, more importantly, to identify strategies to halt the formation of secondary nucleation, which could be key to developing effective disease-modifying therapies for PD.

Like other neurodegenerative diseases, PD exhibits selective neuronal vulnerability[9], and single-cell RNA sequencing (scRNA-seq) studies have identified distinct neuronal subtypes that are more susceptible to degeneration in PD[40,41]. In this study, we successfully demonstrated the ability to deliver SAS into specific neuron types non-invasively using AAV-PHP.eB. By targeting different

neuronal subpopulations using cell-type-specific Cre lines or promoters, we can systematically investigate the role of diverse neuronal population in PD pathology. This approach provides a powerful strategy to dissect the contributions of specific neuronal populations to disease progression, offering insights into why certain neurons are particularly susceptible and identifying potential therapeutic targets to protect these vulnerable populations.

αSyn aggregation is not only a hallmark of PD, but is also implicated in other synucleinopathies, such as dementia with Lewy bodies (DLB) and multiple system atrophy (MSA)[8]. The SAS system can be readily extended to study these disorders, investigating potentially distinct or overlapping pathological mechanisms. More broadly, this innovative synthetic biology approach can be extended to model other neurodegenerative diseases characterized by abnormal protein aggregation. By modifying the SAS system to drive the intracellular aggregation of other disease-associated proteins, such as Tau in Alzheimer's disease and TDP-43 in amyotrophic lateral sclerosis, we can develop highly controllable and tunable models for disease studies and therapeutic discovery. Combining these models, this approach could provide a comprehensive framework to uncover both shared and disease-specific mechanisms of neurodegeneration and facilitate large-scale drug screening, accelerating the identification of therapeutic interventions to halt disease progression.

Methods

Animals

Animal husbandry and experimental procedures involving mice were done in accordance with protocols approved by the California Institute of Technology Institutional Animal Care and Use Committee (IACUC, protocol 1650) and the mice were handled in accordance with the principles and procedures of the Guide for the Care and Use of Laboratory Animals of the National Institutes of Health. Mice were group housed at 2-3 mice per cage with 13/11 light/dark cycles at ambient temperatures of 71–75 °F and 30–70% humidity. C57BL/6J (Jackson Labs #026267), $Snca^{tm1.1Kluk/J}$ (Jackson Labs #035412) and heterozygous $B6.Cg\text{-}7630403G23Rik^{Tg(Th\text{-}cre)1Tmd/J}$ (Jackson Labs #008601) mice were used in experiments. Genotyping was performed by Transnetyx. AAVs were administered via retro-orbital injection during isoflurane anesthesia (1-3% in 95% O2/5% CO2, provided by nose cone at 1 L/min), at 1×10^{12} viral genomes (v.g.) per animal. A detailed protocol for systemic AAV administration through retro-orbital injection is available on protocols.io (dx.doi.org/10.17504/protocols.io.36wgqnw73gk5/v1). Mice were randomly assigned to different conditions.

Cell lines

HEK 293 cells (ATCC, CRL-3216) were used in SAS screening and characterization. The human embryonic stem cell line (hESC) line CSES07 (Cedars Sinai, CVCL_B818) was used to derive both monolayer neurons and organoids. CSES07 was obtained from Cedars Sinai Medical Center with a verified normal karyotype and was contamination-free. All cell lines were authorized for

use under the supervision of the California Institute of Technology Institutional Biosafety Committee (IBC #22-182).

SAS screening in HEK cells

SAS plasmids were transfected into HEK cells using Lipofectamine 3000 (ThermoFisher, L3000008) following the manufacture's instruction. Briefly, 100K HEK cells were plated in 24-well plates. The next day, 0.4 µg SAS plasmids and 0.1 µg rtTA plasmids were transfected into each well. Cells were incubated with lipofectamine overnight. The medium was switched to 5% FBS in DMEM/F12 the next morning, and 10 µg/ml of doxycycline (Sigma, Cat # D9891-10G) was added into the medium. After 3 days of doxycycline treatment, cells were fixed and stained. Detailed information on SAS constructs is listed in Supplemental Table 1.

For protocol, see **dx.doi.org/10.17504/protocols.io.6qpvr97wzvmk/v1**

Immunostaining of cultured cells

At predetermined time points, cells were removed from the incubator, washed once with phosphate-buffered saline (PBS), and fixed with 4% paraformaldehyde for 10 minutes at room temperature (RT). After washing 3 times with PBS, the blocking buffer containing 1xPBS, 0.03% Triton X-100 (PBST), and 5% normal donkey serum was applied and incubated at RT for 60 minutes. Primary antibodies were diluted in fresh blocking buffer, added on the cell, and incubated overnight at 4°C. The next day, the antibody solution was washed off with PBST for 10 minutes, 3 times. Secondary antibodies were applied for 60 minutes and then washed off with PBST for 10 minutes, 3 times. After the final wash, cells remain in PBST for imaging. Antibodies and reagents used were listed in the key resource table.

For protocol, see **dx.doi.org/10.17504/protocols.io.4r3l29eb4v1y/v1**

Western blotting

Western blot was performed using the iBind Automated Western Systems following manufacture's instructions. Briefly, cells were collected with cold DPBS and lysated with RIPA buffer. Total protein concentration was measured using Qubit Protein BR Assay kit and Qubit4. An equal amount of protein was run in Bio-Rad 4-20% TGX stain-free gels and then transferred to the PVDF membrane. Membranes were fixed with 4% paraformaldehyde for 10 minutes before blotting. Protein immunodetection was performed with desired antibodies using iBind Automated Western Systems. Antibodies information was listed in key resources tables. Signals were detected with Max Western ECL and imaged by the ChemiDoc imaging system. The reagents used were listed in the key resource table.

For protocol, see **dx.doi.org/10.17504/protocols.io.j8nlk96p6v5r/v2**

Viral vector production

AAV packaging and purification were carried out as previously described[42]. The viruses for *in vitro* experiments were produced by suspension HEK cells. In brief, recombinant AAV was

produced by triple transfection of cells in suspension using the VirusGEN AAV Kit with RevIT enhancer (Mirus Bio, MIR 8007) at a molar ratio of transgene: AAV capsid: pHelper = 1:2:0.5, as per the manufacturer's instructions. The total DNA amount was 2 µg per mL of cells. Virus-producing cells and medium were harvested 72 hours post-transfection. The viruses used in animal experiments were produced by adherent HEK cells. In brief, HEK cells are transiently transfected using polyethyleneimine (PEI) at a molar ratio of transgene: AAV capsid: pHelper = 1:4:2). 120-hours after transfection, the producer cells were harvested, and cell culture media was collected at 72- and 120-hours post-transfection. Following cell lysis and nuclease digestion, viruses from suspension cells and adherent cells were purified using iodixanol step gradient columns followed by ultracentrifugation, as previously detailed[42]. The purified AAVs were quantified through droplet digital PCR (ddPCR) following Addgene's protocol with modifications[43]. Briefly, AAV samples were first serially diluted to achieve a suitable concentration for ddPCR analysis. The PCR reaction mixture was prepared using ddPCR EvaGreen Supermix (Bio-Rad), primers for WPRE or ITRs, the diluted AAV sample, and nuclease-free water. The mixture was then partitioned into droplets using the QX200 Droplet Generator, and the droplets were transferred to a 96-well plate for PCR in a thermocycler. After cycling, the droplets were read using a QX200 Droplet Reader, and the concentration of the viral genome was analyzed using QuantaSoft software. The viral genome titer in original sample was then back calculated using the dilution factors. The final viral preparation is stored in DPBS with Pluronic F-68 to prevent adhesion loss. The reagents used were listed in the key resource table.
For protocol, see **dx.doi.org/10.17504/protocols.io.ewov1dpeovr2/v1**

Primary neuron preparation

The day before the procedure, HBSS 10x (Thermo Fisher, Cat # 14065056) was diluted to 1x using sterile distilled water (Invitrogen, Cat # 10977015) and pre-cold at 4 °C. Glass inserts (Neuvitro Corporation, Cat # GG-12-15 Pre) were placed in 24-well plates and were coated with Poly-D-lysine (Millipore Sigma, Cat # A-003-E) overnight. Plating media was prepared using BrainPhys Neuronal Medium SM1 Kit (Stem Cell Technologies, Cat # 05792), 1× Glutamax, (Thermo Fisher,Cat # 35050061), 1× Penicillin-Streptomycin (Thermo Fisher, Cat # 15140122,), and 1× l-glutamine (Bio-Techne, Cat # 0218). Pregnant mice from JAX were euthanized on day 17 of pregnancy. Embryos were removed, decapitated, and brains were isolated in cold HBSS. Cortices and hippocampi were dissected, and hippocampi were quartered and placed into 15 ml tubes. Papain (Sigma Aldrich, Cat # P3125-250MG) was added for digestion, followed by washing with a stopping medium containing HBSS 1× and 10% Fetal Bovine Serum. Hippocampi were dissociated by gentle pipetting, and supernatants with dissociated neurons were collected. After centrifugation, cells were resuspended in plating media, counted, and seeded at 200,000 cells/well on Poly-D-lysine-coated inserts. After 72 hours, the media was replaced with a combination of 500 ml Neurobasal Medium (Thermo Fisher, Cat # 21103049), 2 mL B27 Supplement (Thermo

Fisher, Cat # 17504044), and 0.5 mM L-glutamine (Bio-Techne, Cat # 0218). SAS 3 virus was then added for predetermined times and doses.
For protocol, see http://dx.doi.org/10.17504/protocols.io.5qpvo98ozv4o/v1 .

Cortical neurons and organoid differentiation

hESC were plated on 6-well plate coated with Vitronectin (Gibco, Cat # A14700) at 1:100 diluted in DPBS (Gibco, Cat #14190250) and maintained in E8 medium (Thermo Fisher, Cat #A1517001). The E8 medium was changed every day, and the cells were passaged every 3-5 days at 70-85% confluence. The cells were passaged using EDTA dissociation as described previously[44]. For inducing differentiation, hESCs were dissociated at 70%-80% confluence using EDTA dissociation buffer and replated as a single cell suspension on Matrigel-coated 24-well plates at a density of 100K cells/cm2 in E6 medium (Thermo Fisher, Cat #A1516401) containing 10 μM ROCK-inhibitor (Y-27632; R&D, Cat #1254). The cells were kept in E6 medium + Y-27632 overnight. The next day, the medium was switched to a neuroectoderm-inducing medium. The cells were kept in E6 medium containing 10 μM SB431542 (R&D, Cat #1614), 100nM LDN139189 (R&D, Cat #6053), and 500nM XAV (R&D, 3748) for the first 4 days and then switched to E6 medium containing 10 μM SB and 100nM LDN for 6 days. Then the cells were switched to progenitor expanding medium, containing neurobasal (NB) medium supplemented with l-glutamine (Gibco, Cat #25030-164), N2 (Stem Cell Technologies, 07156), B27 (Life Technologies, Cat #17504044) and NEAA (Sigma, Cat #M7145) for 10 days. At D20, the neuron progenitors were dissociated into single cells and replated into a V-bottom ultra-low attachment 96-well plate at 100K per well to form neuron spheres. After 4 days, the spheres were transformed to low attachment 10 cm dishes and placed on a shaker for long-term culture and maturation in cortical neuron medium containing NB/N2/B27/Glu/NEAA, ascorbic acid (200μM, Sigma, 4034-100g), dbcAMP (500 μM, Sigma, Cat #D0627), BDNF (20ng/mL, R&D, Cat #248-BDB) and GDNF (20ng/mL, Peprotech, Cat #450-10)[45]. Organoids are cultured in suspension for 90 days before adding viruses.
For protocol, see **dx.doi.org/10.17504/protocols.io.3byl4wrzovo5/v1**

Open field test (OFT)

Mice were tested in the OFT bi-weekly. The open-field apparatus consisted of four-square arenas (27 cm × 27 cm), with a camera (EverFocus, EQ700) placed 1.83 m above the floor of the arenas. EthoVision XT was used to capture and subsequently analyze animal locomotion. Each trial consisted of a 2 min habituation period, followed by a 10 min test period. To avoid confounds due to odors from non-cagemates, only animals from the same cage were recorded simultaneously. Behavior equipment was disinfected and deodorized between each animal. The distance traveled over the course of the experimental period was determined.
For protocol, see **dx.doi.org/10.17504/protocols.io.5qpvo972xv4o/v1**

Whole gut transit assay

A solution of 0.5% methylcellulose and 6% carmine red (Millipore Sigma, Cat # C1022-25G) was prepared, autoclaved, and administered via a 20 ga flexible plastic oral gavage (Instech, Cat # FTP 20-30). Fecal pellets were monitored every 15 minutes for the appearance of carmine red to determine whole gut transit time, defined as the interval from gavage to the first appearance of red in the stool. Fecal pellets were collected, weighed, dried overnight at 65°C, and reweighed to calculate total weight and water content.

For protocol, see **dx.doi.org/10.17504/protocols.io.3byl4wxd2vo5/v1**

Beam crossing assay

To measure skilled locomotion using the narrowing beam assay, a clear plexiglass beam consisting of three 25 cm segments (widths 3.5 cm, 2.5 cm, and 1.5 cm) was elevated above the table surface using empty clean cages. At the narrow end, an empty cage was placed on its side, and bedding from the animal's home cage was placed inside. A white light was also placed over the broad end to motivate animals to move across the beam. For each trial, animals were placed at the end of the widest segment, with all 4 limbs touching the beam surface. Each trial was recorded with a video camera placed to the side and perpendicular to the beam's length, affording a view of both left and right hindlimbs. A trial was considered complete once the animal had traversed the beam, without turning around, and entered the goal cage. Once an animal had completed three trials, the session was completed. Beam crossing was analyzed using BORIS software, measuring the time taken to cross the beam and the number of foot slips.

For protocol, see **dx.doi.org/10.17504/protocols.io.n92ldr2jxg5b/v1**

Tissue harvesting and processing

Animals were transcardially perfused with 30 mL of ice-cold heparinized 1× PBS, and brains were dissected. One hemisphere of the brain was used for RNAseq. For analysis of fluorescent protein expression, one hemisphere of the brain was submerged in ice-cold 4% PFA formulated in 1× PBS and fixed for 24-48 hr at 4 °C. Brains were subsequently cryoprotected at 4°C in a solution containing 30% (w/v) sucrose for 72 hr. Brains were flash-frozen in O.C.T. Compound (Scigen, Cat # 4586) using a dry ice-ethanol bath and kept at -80 °C until sectioning.

For protocol, see **dx.doi.org/10.17504/protocols.io.ewov1d5xovr2/v1**.

Immunostaining of mouse tissue

Brain was sliced at 100 µm using a cryostat (Leica Biosystems, CM1950) and collected in 1× PBS. Sections were stored in PBS supplemented with 0.02% Azide.

For protocol, see **dx.doi.org/10.17504/protocols.io.x54v9rkzpv3e/v1**.

For immunostaining, brain sections were blocked with 5% normal donkey serum in 0.1 % PBST for 90 mins and then incubated with primary antibody solution prepared in 0.1 % PBST supplemented with 5% normal donkey serum overnight on a shaker at 4°C. After washing in 0.1 % PBST (3 × 30 min), the sections were incubated with secondary antibodies overnight on a shaker at 4°C and then washed 3 x 30 min in 0.1 % PBST. The tissues were mounted on glass slides with

Prolong Diamond Antifade mounting media (Thermo Fisher Scientific, Cat # P36970). Imaging was performed with a spinning disk confocal microscope. Antibodies are listed in the Key Resource Table (Table S4).
For protocol, see https://dx.doi.org/10.17504/protocols.io.kqdg3q7ypv25/v1

RNA extraction

RNA extraction from cells was performed using the Direct-zol RNA Miniprep kit (Zymo, Cat # R2051). Briefly, the cells were removed from incubator, washed once with DPBS, then 350 µL of trizol was added directly to each well to collect the cells. Subsequent RNA extraction was done following the manufacturer's instructions.
For protocol, see **dx.doi.org/10.17504/protocols.io.6qpvr9r2zvmk/v1**

RNA extraction from organoids were performed using the QIAshredder kit (Qiagen, Cat # 79654) and miRNeasy Mini Kit (Qiagen Cat # 217004). Briefly, 3 organoids were harvested for each RNA extraction and 350 µL of Buffer RLT from RNeasy Mini Kit + 3.5 µL β-mercaptoethanol (β-ME) were added to lyse the organoid. Subsequent RNA extraction was done following the manufacturer's instructions.
For protocol, see **dx.doi.org/10.17504/protocols.io.81wgbr95qlpk/v1**

RNA extraction from mice brain tissue was performed using the miRNeasy Mini Kit (Qiagen catalog, Cat # 217004) on a QIAcube Connect (Qiagen). After perfusion with cold PBS, the entire olfactory bulb was dissected and placed in TRIzol directly and processed immediately for RNA extraction following manufacturer's instructions.
For protocol, see **dx.doi.org/10.17504/protocols.io.eq2ly618pgx9/v1**.

RNA sequencing (RNA-seq)

Bulk RNAseq was performed by the Millard and Muriel Jacobs Genetics and Genomics Laboratory at California Institute of Technology. RNA integrity was assessed using the RNA 6000 Pico Kit for Bioanalyzer (Agilent Technologies, Cat # 5067-1513), and mRNA was isolated from ~1 µg of total RNA using NEBNext Poly(A) mRNA Magnetic Isolation Module (NEB, Cat #E7490). RNA-seq libraries were constructed using the NEBNext Ultra II RNA Library Prep Kit for Illumina (NEB, Cat. No. / ID: E7770) following the manufacturer's protocols. Briefly, mRNA was fragmented to an average size of 200 nt by incubating at 94°C for 15 min in the first strand buffer. cDNA was then synthesized using random primers and ProtoScript II Reverse Transcriptase followed by second strand synthesis using NEB Second Strand Synthesis Enzyme Mix. The resulting DNA fragments were end-repaired, dA-tailed and ligated to NEBNext hairpin adaptors (NEB, Cat. No. / ID: E7335). Following ligation, adaptors were converted to the "Y" shape by treating with USER enzyme, and DNA fragments were size selected using Agencourt AMPure XP beads (Beckman Coulter # A63880) to generate fragment sizes between 250-350 bp. Adaptor-ligated DNA was PCR amplified followed by AMPure XP bead clean up. Libraries were

quantified using a Qubit dsDNA HS Kit (ThermoFisher Scientific, Cat. No. / ID: Q32854), and the size distribution was confirmed using a High Sensitivity DNA Kit for Bioanalyzer (Agilent Technologies, Cat. No. / ID: 5067- 4626). Libraries were sequenced on an Illumina NextSeq2000 in paired end mode with a read length of 50 nt and sequencing depth of 25 million reads per library. Base calls and FASTQ generation were performed with DRAGEN 4.2.7.

Transcriptomics data analysis

Raw sequencing reads were processed and aligned by Rsubread package v2.16.1 (https://bioconductor.org/packages/release/bioc/html/Rsubread.html, RRID:SCR_016945) in R (v4.3.2) to align trimmed reads. For human cortical organoids, reads were aligned to the GRCh38.p14 reference genome, while mouse brain tissues were aligned to the GRCm39 reference genome. The corresponding gene annotation files (GTF) were used with featureCounts (https://subread.sourceforge.net/featureCounts.html, RRID:SCR_012919) to generate gene level counts for each dataset. Data were subsequently normalized with DESeq2 v1.42.1 (https://bioconductor.org/packages/release/bioc/html/DESeq2.html, RRID:SCR_015687) and principal coordinate analysis was subsequently performed by multidimensional scaling to assess sample level clustering using the limma package (v3.60.4, RRID:SCR_010943). DESeq2 was then used to assess differential gene expression between rtTA and SAS3 samples. A two-tailed false discovery rate (FDR) < 0.05 (original Benjamini-Hochberg method) determined statistical significance and $|\log2(FC)| > 1.0$ was selected to identify differentially expressed genes (DEGs). Pathway analysis by statistical overrepresentation was performed with DEGs separately for upregulated and downregulated genes with the Gene Ontology (GO) database using the Rapid Integration of Term Annotation and Network (RITAN) package v1.26.0577 (https://bioconductor.org/packages/release/bioc/html/RITAN.html). A two-sided adjusted p-value (q-value) threshold of 0.05 (Benjamini-Hochberg method) was used to determine statistically overrepresented pathways.

Quantification and statistical analysis

Data are presented as mean ± SEM and were derived from at least three independent experiments. Information on replicates (n) is given in figure legends. Statistical analysis was performed using the unpaired t-test, also known as Student's t-test (comparing two groups) or ANOVA with Dunnett test (comparing multiple groups against control). Distribution of raw data approximated normal distributions.

Resource availability

The data, code, protocols, and key lab materials used and generated in this study are listed in a Key Resource Table alongside their persistent identifiers at Table S4. The bulk transcriptomics data generated and analyzed in this study have been deposited in the NCBI Sequence Read Archive (SRA) under BioProject accession number PRJNA1227536. The raw sequencing data and

associated metadata are publicly available and can be accessed via the NCBI SRA database at https://www.ncbi.nlm.nih.gov/bioproject/PRJNA1227536. All code associated with analysis and plotting are available from https://github.com/jdthoang/FanY_2025_SAS

Acknowledgments

We thank Dr. Catherine Oikonomou for the comprehensive editing of the manuscript. We thank Patricia Anguiano and Elisha Mackey for logistical assistance, and the entire Gradinaru laboratory for critical feedback on the research and manuscript. This work was supported by the Office of Laboratory Animal Resources, CLOVER Center, and Millard and Muriel Jacobs Genetics and Genomics Laboratory at California Institute of Technology. Figures contain images created with BioRender.com. Y.F. is supported by Chen Postdoc Innovator Grant. This research was funded by Aligning Science Across Parkinson's (ASAP-020495 to V.G.) through the Michael J. Fox Foundation for Parkinson's Research (MJFF). For the purpose of open access, the author has applied a CC BY public copyright license to all Author Accepted Manuscripts arising from this submission.

Author contributions

Y.F. conceived the project, wrote the manuscript and prepared figures with input from all authors. G.M.C., C.S., J.D.H. and V.G. assisted in manuscript preparation. Y.F. performed most experiments and collected and analyzed the data. J.D.H. performed the analysis of all RNA-seq data and contributed to animal experiments. C.S. performed all behavior assays, contributed to primary neuron, RNA-seq and histology experiments, and assisted in many experiments. Y.B. contributed to cloning, RNA-seq and organoid experiments. S.D. contributed to primary neuron and histology experiments. G.M.C. contributed to animal experiments. N.A. contributed to cloning and virus production. X.D. contributed to design of constructs. C.L. contributed to western blotting. Z.Q. contributed to virus production. V.G. supervised all aspects of this study and funded the project.

Declaration of interests

V.G. is a co-founder and member of the board of directors of Capsida Therapeutics, a fully integrated AAV engineering and gene therapy company. The remaining authors declare no competing interests.

Inclusion and diversity

We support inclusive, diverse, and equitable conduct of research.

References:

1. Ross, C. A. & Poirier, M. A. Protein aggregation and neurodegenerative disease. *Nat Med* **10**, S10–S17 (2004).
2. Soto, C. & Pritzkow, S. Protein misfolding, aggregation, and conformational strains in neurodegenerative diseases. *Nat Neurosci* **21**, 1332–1340 (2018).
3. Goedert, M., Clavaguera, F. & Tolnay, M. The propagation of prion-like protein inclusions in neurodegenerative diseases. *Trends in Neurosciences* **33**, 317–325 (2010).
4. Jucker, M. & Walker, L. C. Self-propagation of pathogenic protein aggregates in neurodegenerative diseases. *Nature* **501**, 45–51 (2013).
5. Spillantini, M. G., Crowther, R. A., Jakes, R., Hasegawa, M. & Goedert, M. α-Synuclein in filamentous inclusions of Lewy bodies from Parkinson's disease and dementia with Lewy bodies. *Proceedings of the National Academy of Sciences* **95**, 6469–6473 (1998).
6. Del Rey, N. L.-G. *et al.* Advances in Parkinson's Disease: 200 Years Later. *Frontiers in Neuroanatomy* **12**, (2018).
7. Postuma, R. B. & Berg, D. Advances in markers of prodromal Parkinson disease. *Nat Rev Neurol* **12**, 622–634 (2016).
8. Calabresi, P. *et al.* Alpha-synuclein in Parkinson's disease and other synucleinopathies: from overt neurodegeneration back to early synaptic dysfunction. *Cell Death Dis* **14**, 1–16 (2023).
9. Surmeier, D. J., Obeso, J. A. & Halliday, G. M. Selective neuronal vulnerability in Parkinson disease. *Nat Rev Neurosci* **18**, 101–113 (2017).
10. Jackson-Lewis, V., Blesa, J. & Przedborski, S. Animal models of Parkinson's disease. *Parkinsonism Relat Disord* **18 Suppl 1**, S183-185 (2012).
11. Konnova, E. A. & Swanberg, M. Animal Models of Parkinson's Disease. in *Parkinson's Disease: Pathogenesis and Clinical Aspects* (eds. Stoker, T. B. & Greenland, J. C.) (Codon Publications, Brisbane (AU), 2018).
12. Dovonou, A. *et al.* Animal models of Parkinson's disease: bridging the gap between disease hallmarks and research questions. *Translational Neurodegeneration* **12**, 36 (2023).
13. Bové, J. & Perier, C. Neurotoxin-based models of Parkinson's disease. *Neuroscience* **211**, 51–76 (2012).
14. Bové, J., Prou, D., Perier, C. & Przedborski, S. Toxin-induced models of Parkinson's disease. *Neurotherapeutics* **2**, 484–494 (2005).
15. Dawson, T. M., Ko, H. S. & Dawson, V. L. Genetic Animal Models of Parkinson's Disease. *Neuron* **66**, 646–661 (2010).
16. Chung, H. K., Ho, H.-A., Pérez-Acuña, D. & Lee, S.-J. Modeling α-Synuclein Propagation with Preformed Fibril Injections. *JMD* **12**, 139–151 (2019).
17. Chmielarz, P. & Domanskyi, A. Alpha-synuclein preformed fibrils: a tool to understand Parkinson's disease and develop disease modifying therapy. *Neural Regeneration Research* **16**, 2219 (2021).
18. Polinski, N. K. A Summary of Phenotypes Observed in the In Vivo Rodent Alpha-Synuclein Preformed Fibril Model. *J Parkinsons Dis* **11**, 1555–1567.

19. Mahul-Mellier, A.-L. *et al.* The process of Lewy body formation, rather than simply α-synuclein fibrillization, is one of the major drivers of neurodegeneration. *Proceedings of the National Academy of Sciences* **117**, 4971–4982 (2020).
20. Shen, H. *et al.* De novo design of self-assembling helical protein filaments. *Science* **362**, 705–709 (2018).
21. Fallas, J. A. *et al.* Computational design of self-assembling cyclic protein homo-oligomers. *Nature Chem* **9**, 353–360 (2017).
22. Garcia-Seisdedos, H., Empereur-Mot, C., Elad, N. & Levy, E. D. Proteins evolve on the edge of supramolecular self-assembly. *Nature* **548**, 244–247 (2017).
23. Chen, Y. X. *et al.* Structural Determination of a Filamentous Chaperone to Fabricate Electronically Conductive Metalloprotein Nanowires. *ACS Nano* **14**, 6559–6569 (2020).
24. Lin, D. *et al.* Time-tagged ticker tapes for intracellular recordings. *Nat Biotechnol* **41**, 631–639 (2023).
25. Linghu, C. *et al.* Recording of cellular physiological histories along optically readable self-assembling protein chains. *Nat Biotechnol* **41**, 640–651 (2023).
26. Chen, X. *et al.* Functional gene delivery to and across brain vasculature of systemic AAVs with endothelial-specific tropism in rodents and broad tropism in primates. *Nat Commun* **14**, 3345 (2023).
27. Shay, T. F. *et al. Human Cell Surface-AAV Interactomes Identify LRP6 as Blood-Brain-Barrier Transcytosis Receptor and Immune Cytokine IL3 as AAV9 Binder*. http://biorxiv.org/lookup/doi/10.1101/2024.01.05.574399 (2024) doi:10.1101/2024.01.05.574399.
28. Makin, S. Pathology: The prion principle. *Nature* **538**, S13–S16 (2016).
29. Goedert, M. Alzheimer's and Parkinson's diseases: The prion concept in relation to assembled Aβ, tau, and α-synuclein. *Science* **349**, 1255555 (2015).
30. Frieg, B. *et al.* Quaternary structure of patient-homogenate amplified α-synuclein fibrils modulates seeding of endogenous α-synuclein. *Commun Biol* **5**, 1–10 (2022).
31. Hartmann, A. Postmortem studies in Parkinson's disease. *Dialogues in Clinical Neuroscience* **6**, 281 (2004).
32. Wakabayashi, K. *et al.* The Lewy Body in Parkinson's Disease and Related Neurodegenerative Disorders. *Mol Neurobiol* **47**, 495–508 (2013).
33. Moors, T. E. & Milovanovic, D. Defining a Lewy Body: Running Up the Hill of Shifting Definitions and Evolving Concepts. *Journal of Parkinson's Disease* **14**, 17 (2024).
34. Kim, T. W. *et al.* TNF-NF-κB-p53 axis restricts *in vivo* survival of hPSC-derived dopamine neurons. *Cell* **187**, 3671-3689.e23 (2024).
35. Fiorini, M. R., Dilliott, A. A., Thomas, R. A. & Farhan, S. M. K. Transcriptomics of Human Brain Tissue in Parkinson's Disease: a Comparison of Bulk and Single-cell RNA Sequencing. *Mol Neurobiol* (2024) doi:10.1007/s12035-024-04124-5.

36. Wang, J. *et al.* Biallelic *FDXR* mutations induce ferroptosis in a rare mitochondrial disease with ataxia. *Free Radical Biology and Medicine* (2025) doi:10.1016/j.freeradbiomed.2025.02.012.
37. Chan, K. Y. *et al.* Engineered AAVs for efficient noninvasive gene delivery to the central and peripheral nervous systems. *Nat Neurosci* **20**, 1172–1179 (2017).
38. Surmeier, D. J. Determinants of dopaminergic neuron loss in Parkinson's disease. *FEBS J* **285**, 3657–3668 (2018).
39. Yang, Y. *et al.* Structures of α-synuclein filaments from human brains with Lewy pathology. *Nature* **610**, 791–795 (2022).
40. Azcorra, M. *et al.* Unique functional responses differentially map onto genetic subtypes of dopamine neurons. *Nat Neurosci* **26**, 1762–1774 (2023).
41. Kamath, T. *et al.* Single-cell genomic profiling of human dopamine neurons identifies a population that selectively degenerates in Parkinson's disease. *Nat Neurosci* **25**, 588–595 (2022).
42. Challis, R. C. *et al.* Systemic AAV vectors for widespread and targeted gene delivery in rodents. *Nat Protoc* **14**, 379–414 (2019).
43. Lock, M., Alvira, M. R., Chen, S.-J. & Wilson, J. M. Absolute determination of single-stranded and self-complementary adeno-associated viral vector genome titers by droplet digital PCR. *Hum Gene Ther Methods* **25**, 115–125 (2014).
44. Fan, Y. *et al.* hPSC-derived sacral neural crest enables rescue in a severe model of Hirschsprung's disease. *Cell Stem Cell* **30**, 264-282.e9 (2023).
45. Lancaster, M. A. & Knoblich, J. A. Generation of cerebral organoids from human pluripotent stem cells. *Nat Protoc* **9**, 2329–2340 (2014).

Figure 1

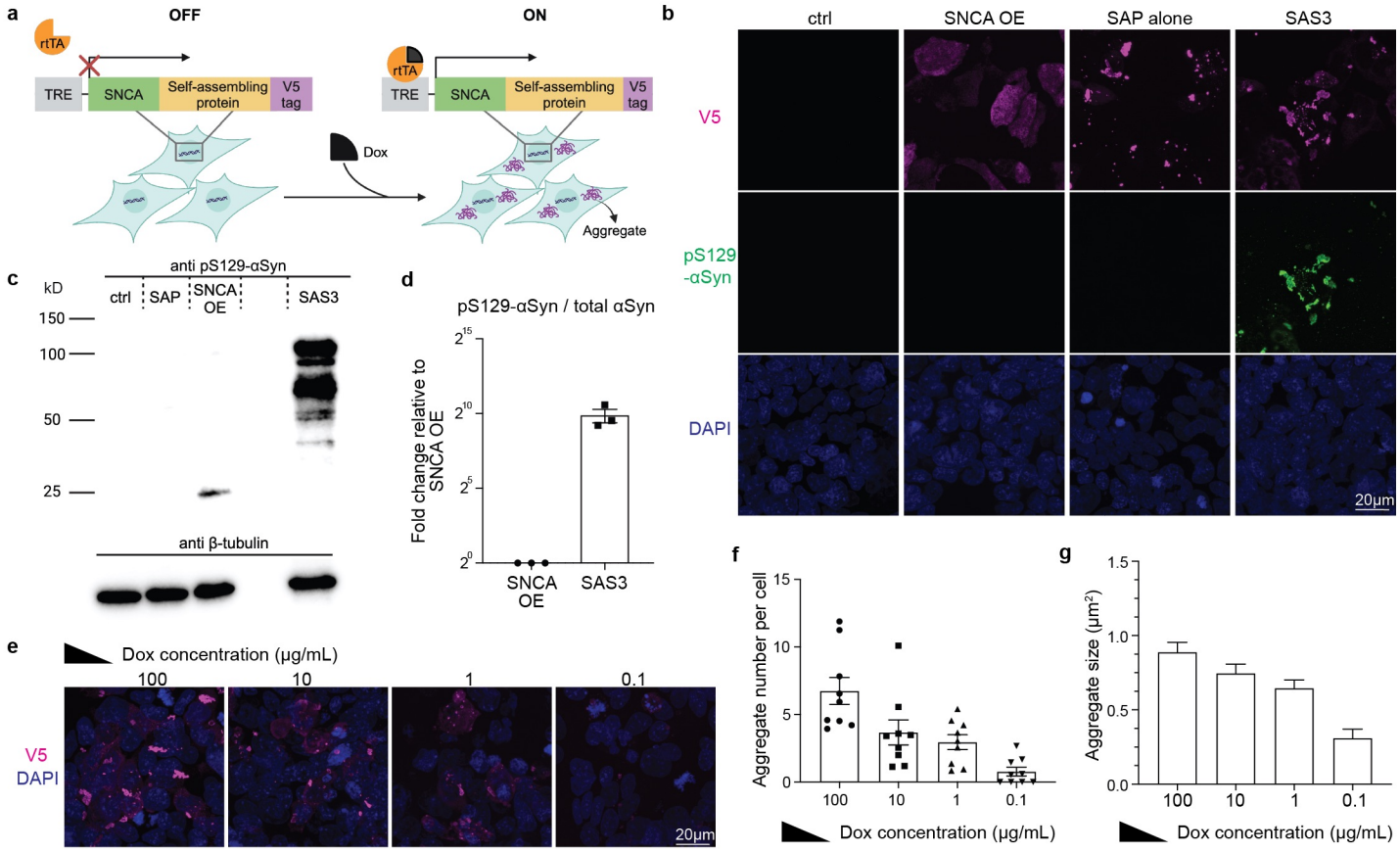
a
OFF
ON
rtTA
TRE
SNCA
Self-assembling protein
V5 tag
Dox
Aggregate
b
ctrl
SNCA OE
SAP alone
SAS3
V5
pS129 -αSyn
DAPI
20μm
c
kD
anti pS129-αSyn
ctrl
SAP
SNCA OE
SAS3
150
100
50
25
anti β-tubulin
d
pS129-αSyn / total αSyn
Fold change relative to SNCA OE
SNCA OE
SAS3
e
Dox concentration (μg/mL)
100
10
1
0.1
V5
DAPI
20μm
f
Aggregate number per cell
Dox concentration (μg/mL)
g
Aggregate size (μm²)
Dox concentration (μg/mL)

Figure 1: Self-assembling synuclein (SAS) drives tunable synucleinopathy.

a, Design of self-assembling synuclein (SAS) system. SAS consists of αSyn fused with a self-assembling protein (SAP). In HEK cells, rtTA expression is drive by the EF1α promoter. Upon dox induction, SAS forms αSyn aggregates intracellularly. **b,** Compared to ctrl (rtTA-transfected only), *SNCA* overexpression (OE) or SAP alone, SAS3 induces αSyn aggregation and strong αSyn S129 phosphorylation after 3 days of dox induction in transfected HEK cells. **c,** Western blot of pS129-αSyn and **d,** quantification show SAS3 induces αSyn aggregation and 1000-fold higher phosphorylation than SNCA OE, indicating its potential to induce PD pathology. n=3 biological replicates. **e,** Immunostaining and quantification of the **f,** number of aggregates per cell and **g,** average aggregate size for different dox concentrations, showing the SAS3 system is tunable. n=9 biological replicates. Scale bars equal 20 μm. Data are presented as mean ± SEM.

Figure 2

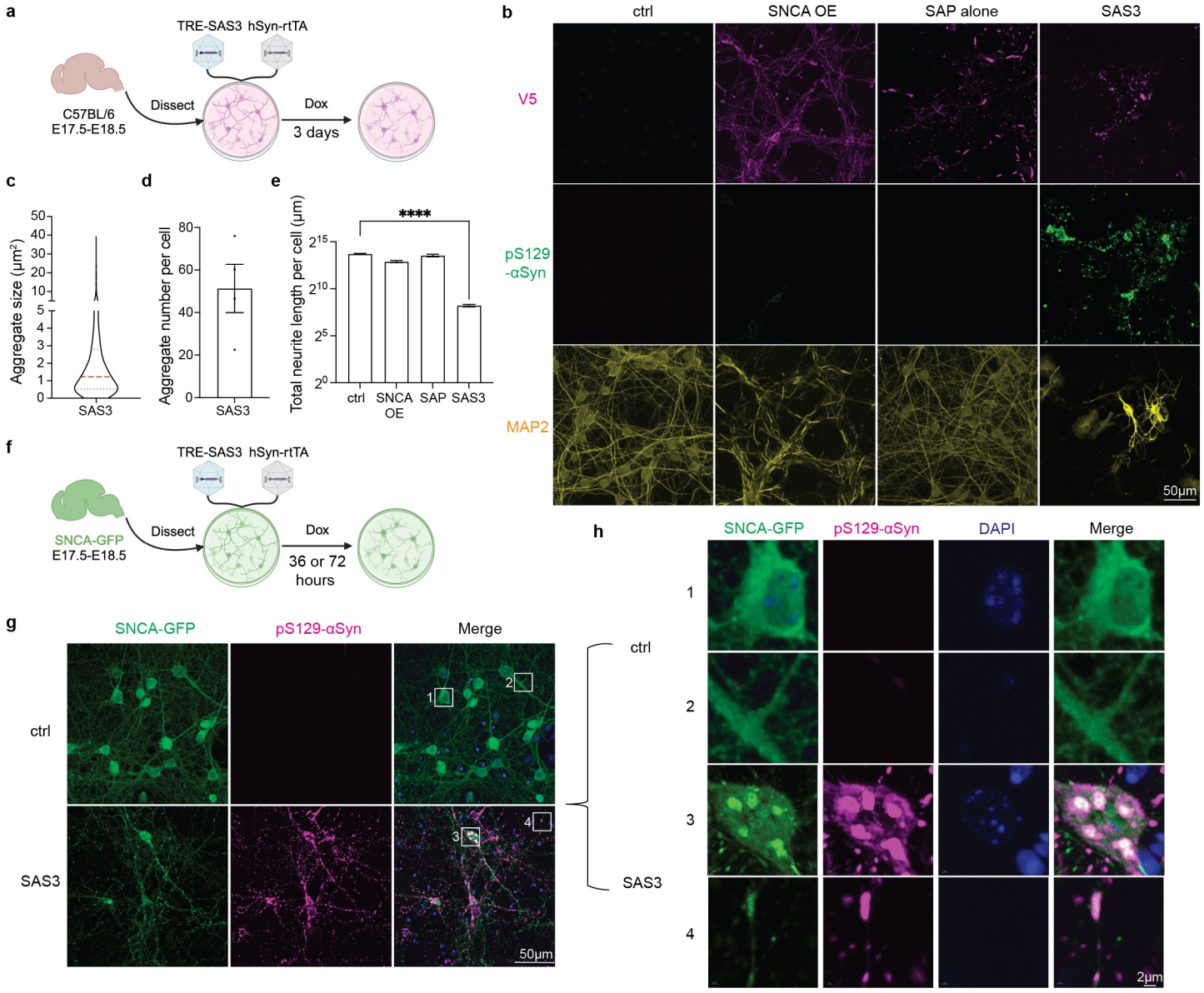
a
TRE-SAS3 hSyn-rtTA
C57BL/6
E17.5-E18.5
Dissect
Dox
3 days
b
ctrl
SNCA OE
SAP alone
SAS3
V5
pS129
-αSyn
MAP2
50μm
c
Aggregate size (μm²)
SAS3
d
Aggregate number per cell
SAS3
e
Total neurite length per cell (μm)
****
ctrl
SNCA OE
SAP
SAS3
f
TRE-SAS3 hSyn-rtTA
SNCA-GFP
E17.5-E18.5
Dissect
Dox
36 or 72 hours
g
SNCA-GFP
pS129-αSyn
Merge
ctrl
SAS3
50μm
h
SNCA-GFP
pS129-αSyn
DAPI
Merge
ctrl
SAS3
2μm

Figure 2: SAS induces neurite retraction and endogenous αSyn aggregation in primary neurons.

a, Experimental design for testing SAS3 in mouse primary neurons. **b,** Immunostaining of V5 tag, pS129-αSyn, and MAP2 in transduced primary neurons after 3 days of dox treatment, showing robust αSyn aggregation and pS129-αSyn in both the soma and neurites of neurons, as well as neurite retraction. **c,** Distribution of aggregate size. **d,** Average number of aggregates per cell**. e,** Quantification of total neurite length per cell. n=4 biological replicates. ****$p<0.0001$. Scale bar equals 50 μm. **f,** Design for testing whether SAS3 can nucleate secondary aggregation of endogenous αSyn in primary neurons carrying the SNCA-GFP reporter. (**g-h**), Immunostaining after 36 hours of dox treatment shows SAS3-induced aggregates contain endogenous αSyn, as shown by GFP signal. Scale bar equals 50 μm in (**g**) and 2 μm in (**h**). Data are presented as mean ± SEM; Statistical analysis was performed using ANOVA with Dunnett test.

Figure 3

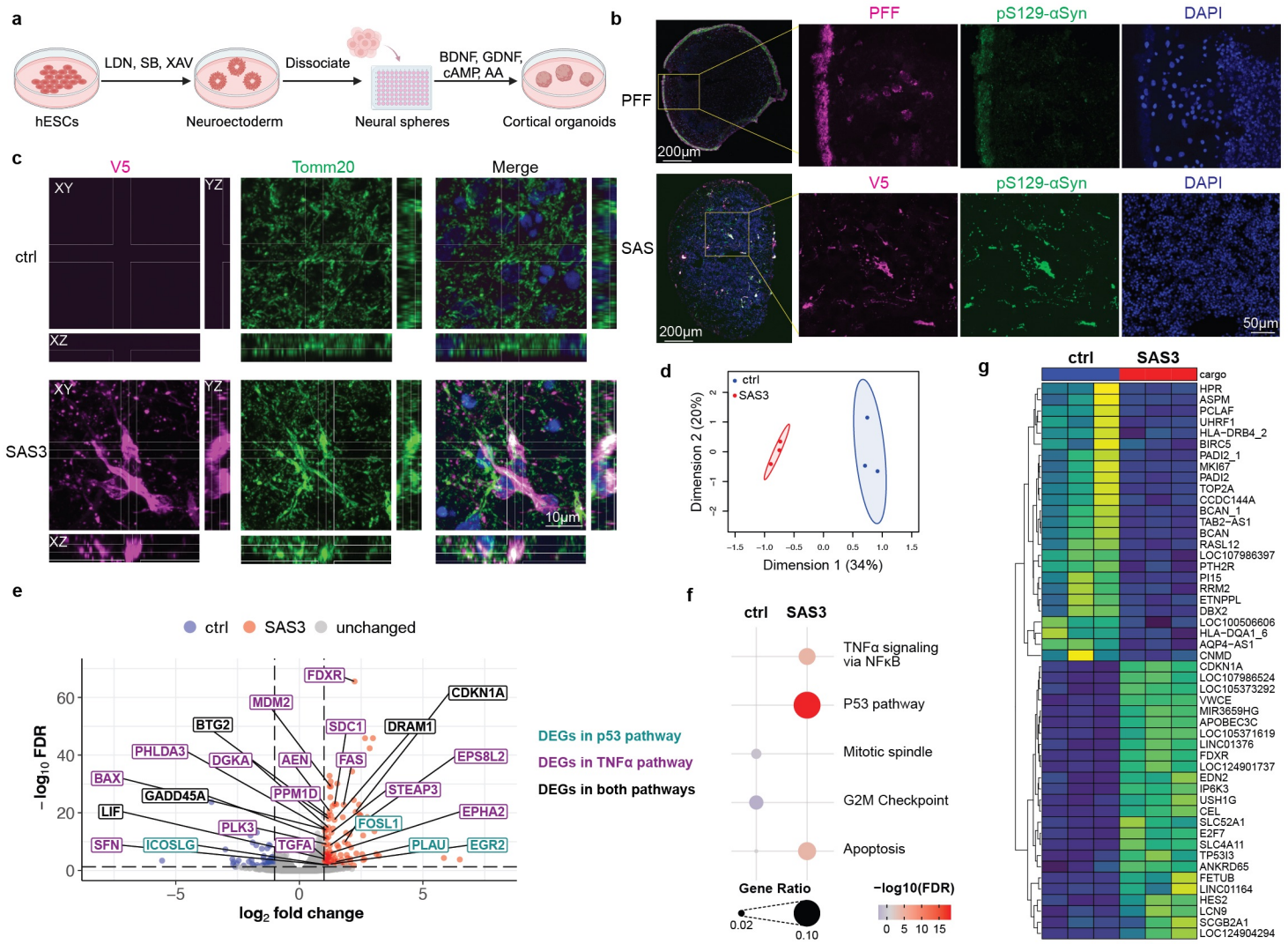
a
LDN, SB, XAV
Dissociate
BDNF, GDNF, cAMP, AA
hESCs
Neuroectoderm
Neural spheres
Cortical organoids
b
PFF
pS129-αSyn
DAPI
PFF
200μm
V5
pS129-αSyn
DAPI
SAS
200μm
50μm
c
V5
Tomm20
Merge
ctrl
SAS3
XY
YZ
XZ
10μm
d
ctrl
SAS3
Dimension 2 (20%)
Dimension 1 (34%)
e
ctrl
SAS3
unchanged
−log10 FDR
log2 fold change
FDXR
MDM2
CDKN1A
BTG2
SDC1
DRAM1
PHLDA3
DGKA
AEN
FAS
EPS8L2
BAX
GADD45A
PPM1D
STEAP3
LIF
EPHA2
PLK3
FOSL1
SFN
ICOSLG
TGFA
PLAU
EGR2
DEGs in p53 pathway
DEGs in TNFα pathway
DEGs in both pathways
f
ctrl
SAS3
TNFα signaling via NFκB
P53 pathway
Mitotic spindle
G2M Checkpoint
Apoptosis
Gene Ratio
0.02
0.10
−log10(FDR)
0
5
10
15
g
ctrl
SAS3
cargo
HPR
ASPM
PCLAF
UHRF1
HLA−DRB4_2
BIRC5
PADI2_1
MKI67
PADI2
TOP2A
CCDC144A
BCAN_1
TAB2−AS1
BCAN
RASL12
LOC107986397
PTH2R
PI15
RRM2
ETNPPL
DBX2
LOC100506606
HLA−DQA1_6
AQP4−AS1
CNMD
CDKN1A
LOC107986524
LOC105373292
VWCE
MIR3659HG
APOBEC3C
LOC105371619
LINC01376
FDXR
LOC124901737
EDN2
IP6K3
USH1G
CEL
SLC52A1
E2F7
SLC4A11
TP53I3
ANKRD65
FETUB
LINC01164
HES2
LCN9
SCGB2A1
LOC124904294

Figure 3: SAS-induced aggregates colocalize with mitochondria and drive neuronal death and inflammation.

a, Schematic of generating human cortical organoids from hESCs. **b,** Immunostaining of fluorescently-labeled PFFs or SAS3 V5 tag and pS129-αSyn in hESC-derived cortical organoids. Unlike PFFs, SAS3 can penetrate and induce PD-like pathology through the entire organoid. Scale bar equals 200 μm and 50 μm in enlargement. **c,** Z-scanning confocal imaging of organoids stained for V5 tag and the mitochondrial marker Tomm20. SAS3-induced aggregates colocalize with mitochondria, shown by XY (main), XZ (bottom panel) and YZ (right panel) projections. Scale bar equals 10 μm. **d,** Principal coordinate analysis (PCoA) shows clear separation of transcriptomic profiles of SAS3 organoids transduced with hsyn-rtTA and TRE-SAS3 using AAV9-X1.1 and control organoids transduced with only hsyn-rtTA. n= 3 biological replicates. **e,** Volcano plot of DEGs with FDR < 0.05 and log2 fold change (FC) >1. Genes belonging to the TNFα pathway are highlighted in magenta, p53 pathway in cyan, and both in black. **f,** Pathway analysis reveals that SAS3-treated organoids contain significantly up-regulated Gene Ontology (GO) pathways associated with apoptosis and inflammation. **g,** Top 25 up and down regulated genes.

Figure 4

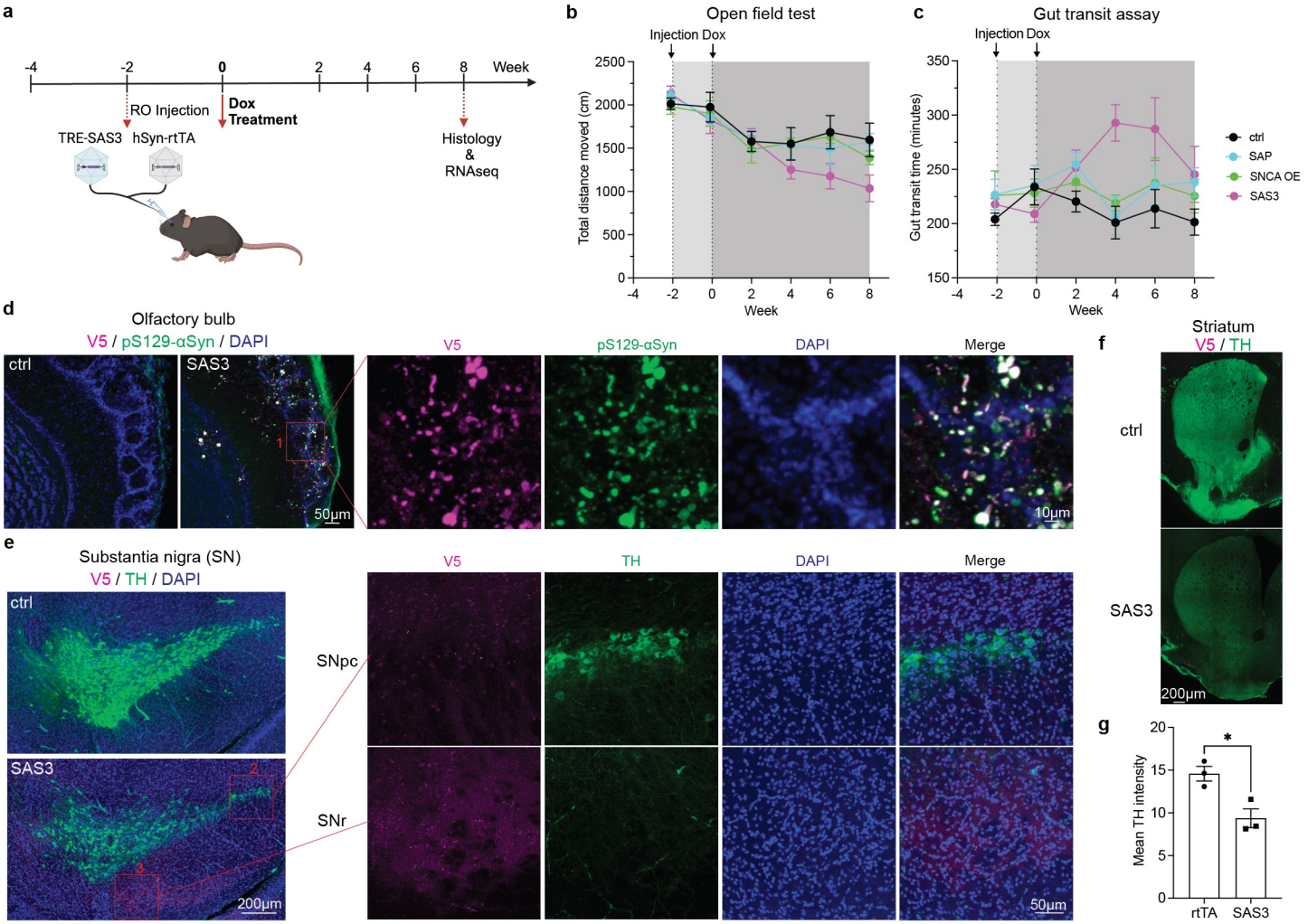
a
-4
-2
0
2
4
6
8
Week
RO Injection
Dox Treatment
TRE-SAS3
hSyn-rtTA
Histology & RNAseq
b
Open field test
Injection Dox
Total distance moved (cm)
Week
c
Gut transit assay
Injection Dox
Gut transit time (minutes)
Week
ctrl
SAP
SNCA OE
SAS3
d
Olfactory bulb
V5 / pS129-αSyn / DAPI
ctrl
SAS3
50μm
V5
pS129-αSyn
DAPI
Merge
10μm
e
Substantia nigra (SN)
V5 / TH / DAPI
ctrl
SAS3
200μm
SNpc
SNr
V5
TH
DAPI
Merge
50μm
f
Striatum
V5 / TH
ctrl
SAS3
200μm
g
Mean TH intensity
rtTA
SAS3

Figure 4: SAS induces PD-relevant histopathology and behavioral deficits in mice.

a, Experimental design for testing SAS3 in WT C57BL/6J mice with AAV-PHP.eB delivered through retro-orbital (RO) injection. Behavioral assays were performed every other week and histology at week 8. **b,** After 4 weeks of dox treatment, SAS3-treated mice exhibit progressively decreased movement in the open field test compared with other groups. n=5 mice. **c,** SAS3-treated mice show increased gut transit time after 4 weeks of dox treatment; the phenotype decreases at 8 weeks. n=5 mice. **d,** Immunostaining for the V5 tag and pS129-αSyn in the olfactory bulb, showing aggregates and strong αSyn phosphorylation. Scale bar equals 50 μm and 10 μm in enlargement. **e,** Immunostaining for the V5 tag and TH in the substantia nigra, showing aggregates in both substantia nigra pars compacta (SNpc) and substantia nigra reticulata (SNr), and a decreased number of TH+ neurons in the SNpc. Scale bar equals 200 μm and 50 μm in enlargement. **f,** Representative images of dopaminergic neuron projections into the striatum. Scale bar equals 200 μm. **g,** Quantification of striatal TH intensity. n=3 mice. Data are presented as mean ± SEM; statistical analysis was performed using the unpaired t-test.

Figure 5

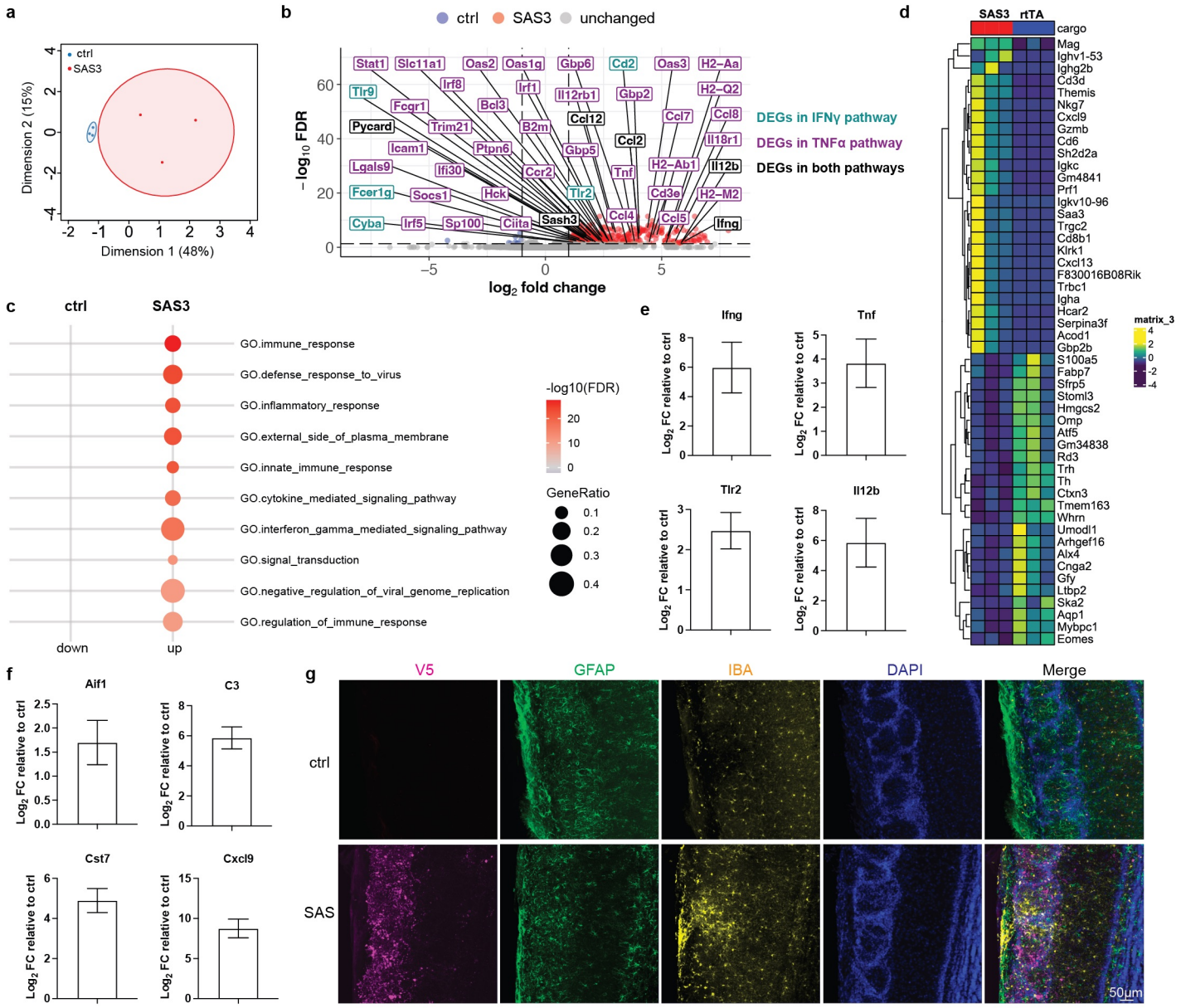
a
ctrl
SAS3
Dimension 2 (15%)
Dimension 1 (48%)
b
ctrl
SAS3
unchanged
−log10 FDR
log2 fold change
DEGs in IFNγ pathway
DEGs in TNFα pathway
DEGs in both pathways
Stat1
Slc11a1
Oas2
Oas1g
Gbp6
Cd2
Oas3
H2−Aa
Tlr9
Irf8
Irf1
Il12rb1
Gbp2
H2−Q2
Fcgr1
Bcl3
Ccl12
Ccl7
Ccl8
Pycard
Trim21
B2m
Ccl2
Il18r1
Icam1
Ptpn6
Gbp5
Lgals9
Ifi30
Ccr2
Tnf
H2−Ab1
Il12b
Fcer1g
Socs1
Hck
Tlr2
Cd3e
H2−M2
Cyba
Irf5
Sp100
Ciita
Sash3
Ccl4
Ccl5
Ifng
c
ctrl
SAS3
GO.immune_response
GO.defense_response_to_virus
GO.inflammatory_response
GO.external_side_of_plasma_membrane
GO.innate_immune_response
GO.cytokine_mediated_signaling_pathway
GO.interferon_gamma_mediated_signaling_pathway
GO.signal_transduction
GO.negative_regulation_of_viral_genome_replication
GO.regulation_of_immune_response
down
up
-log10(FDR)
GeneRatio
e
Ifng
Tnf
Tlr2
Il12b
Log2 FC relative to ctrl
d
SAS3
rtTA
cargo
matrix_3
f
Aif1
C3
Cst7
Cxcl9
Log2 FC relative to ctrl
g
V5
GFAP
IBA
DAPI
Merge
ctrl
SAS
50μm

Figure 5: SAS actives microglia and triggers immune response in mice.

a, PCoA of transcriptomic data shows separation between SAS3-treated mice (transduced with hsyn-rtTA and TRE-SAS3 using PHP.eB) and controls (transduced with only hsyn-rtTA). n= 3 biological replicates. **b,** Volcano plot of DEGs with FDR < 0.05 and log2 fold change (FC) >1. Genes belonging to the TNFα pathway are highlighted in magenta, IFN-γ pathway in cyan, and both in black. **c,** Top 10 significantly altered GO pathways in SAS3-transduced mice indicate up-regulation of pathways involved in inflammation. **d,** Top 25 up and down regulated genes. **e,** Quantification of upregulation of representative genes of the IFN-γ, TNF-α, TLR, and interleukin pathways in SAS3-treated mice compared to controls. **f,** Representative genes involved in microglia activation. **g,** Immunostaining for GFAP and IBA1 in the olfactory bulb, showing activated microglia clustered around SAS-induced aggregates. Scale bar equals 50μm.

Figure 6

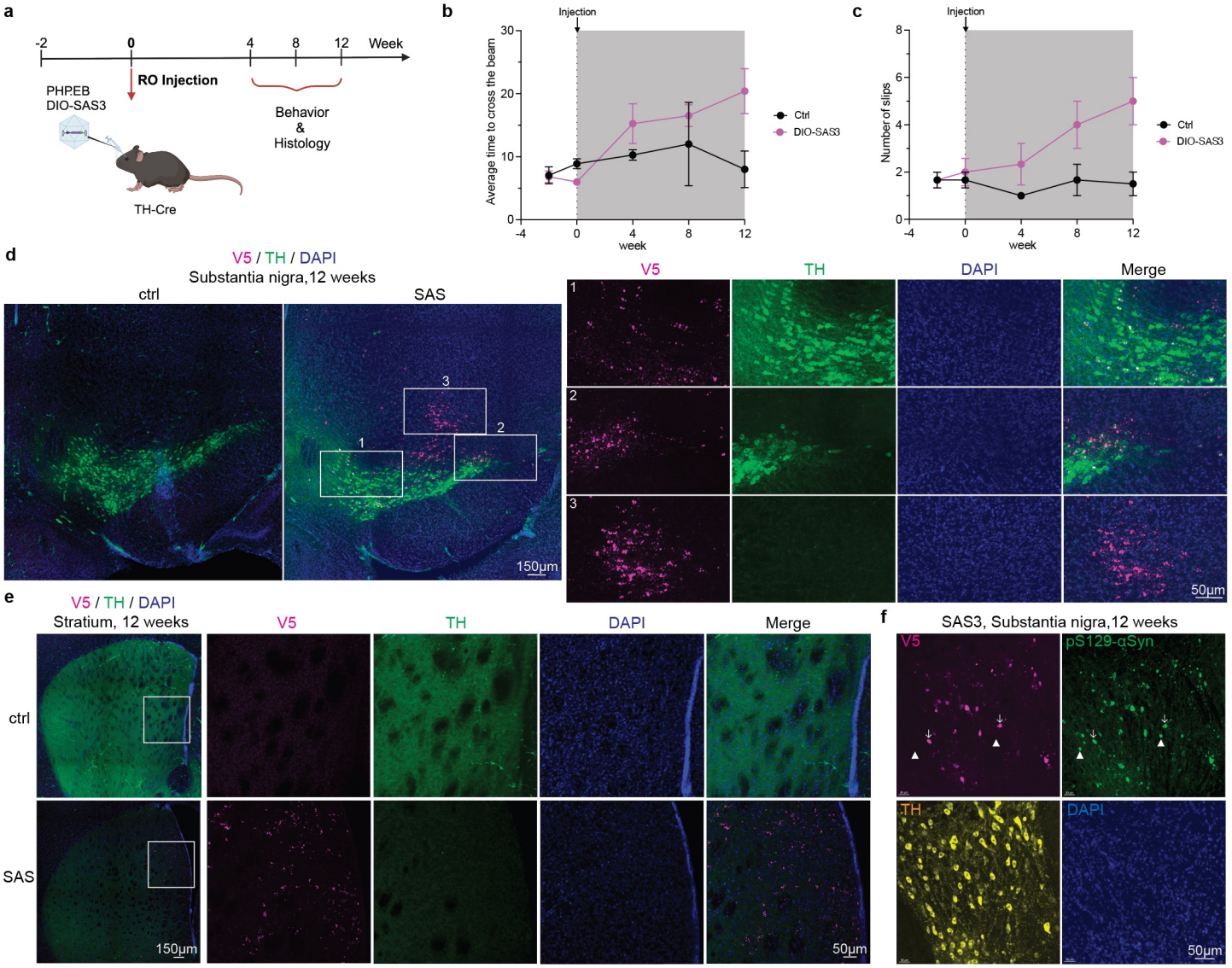
a
-2
0
4
8
12
Week
RO Injection
PHP.EB
DIO-SAS3
TH-Cre
Behavior
&
Histology
b
Injection
Average time to cross the beam
week
Ctrl
DIO-SAS3
c
Injection
Number of slips
week
Ctrl
DIO-SAS3
d
V5 / TH / DAPI
Substantia nigra,12 weeks
ctrl
SAS
150μm
V5
TH
DAPI
Merge
50μm
e
V5 / TH / DAPI
Stratium, 12 weeks
V5
TH
DAPI
Merge
ctrl
SAS
150μm
50μm
f
SAS3, Substantia nigra,12 weeks
V5
pS129-αSyn
TH
DAPI
50μm

Figure 6: Dopaminergic neuron-targeted SAS recapitulates motor deficits and PD histopathology.

a, Experimental design for selectively delivering SAS3 into dopaminergic (DA) neurons. Cre-dependent SAS3 (DIO-SAS3) was RO injected into TH-Cre mice using AAV-PHP.eB. Behavioral assays and histology were performed at 4, 8, and 12 weeks. **b-c,** After 4 weeks of dox treatment, SAS3-treated mice exhibit significant motor impairments in the beam crossing assay, requiring more time to cross the beam (**b**) and displaying more slips (**c**) than controls. n=5 mice. **d,** Immunostaining for the V5 tag and TH in the substantia nigra (SN) region, with enlarged images of the ventral tegmental area (VTA, area 1), SNpc (area 2), and non-TH+ region (area 3). Scale bar equals 150 μm and 50 μm in enlargement. **e,** Immunostaining for the V5 tag and TH in the striatum, suggesting progressive accumulation of aggregates and potential spreading along the nigrostriatal pathway. Scale bar equals 150 μm and 50 μm in enlargement. **f,** Immunostaining for V5, pS129-αSyn, and TH in the SNpc reveals that not only SAS3-expressed proteins (arrows) but also endogenous αsyn (arrowheads) formed aggregates and became phosphorylated. Scale bar equals 50μm.

Figure S1

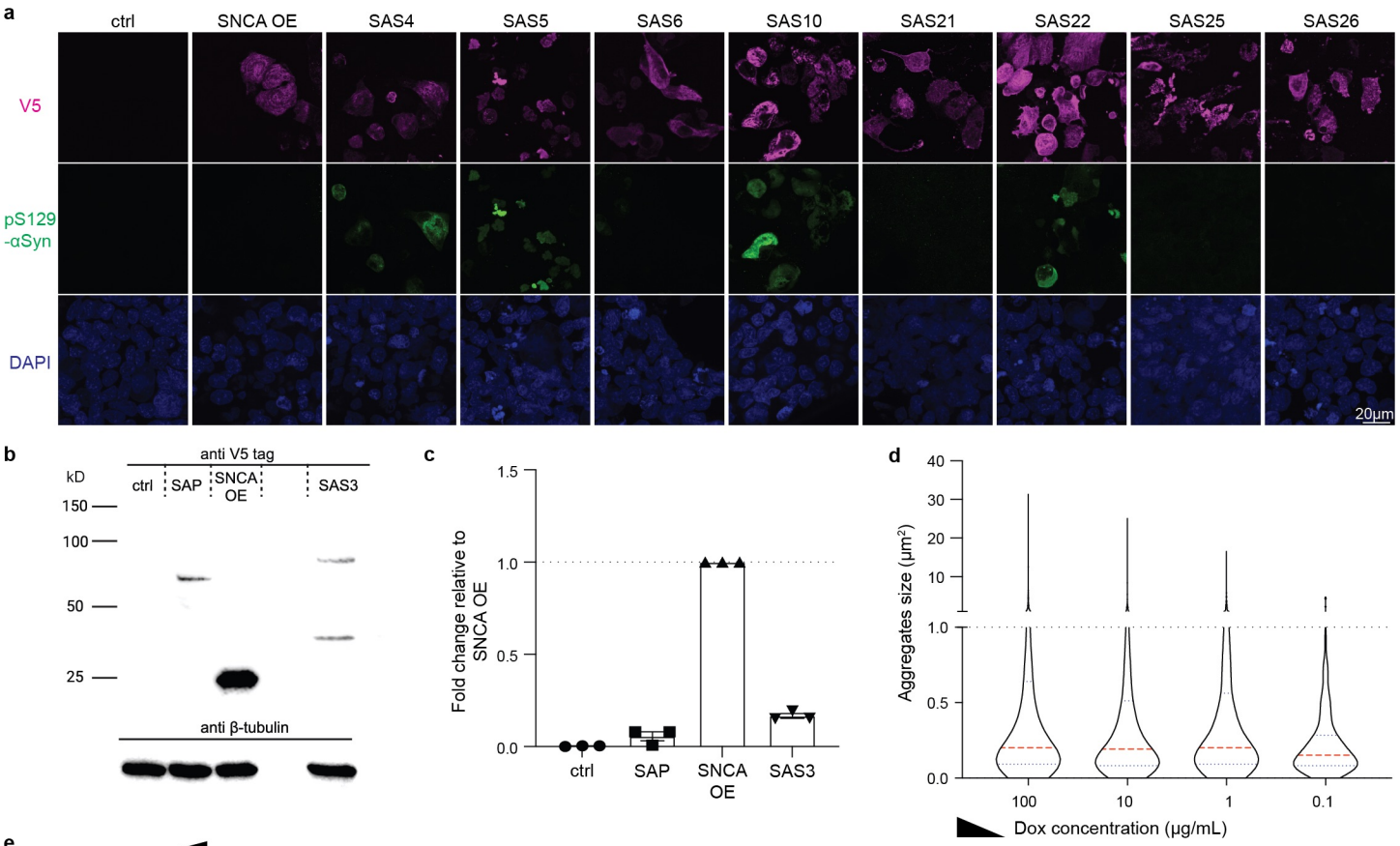
a
ctrl
SNCA OE
SAS4
SAS5
SAS6
SAS10
SAS21
SAS22
SAS25
SAS26
V5
pS129
-αSyn
DAPI
20μm
b
anti V5 tag
kD
ctrl
SAP
SNCA
OE
SAS3
150
100
50
25
anti β-tubulin
c
Fold change relative to
SNCA OE
1.5
1.0
0.5
0.0
ctrl
SAP
SNCA
OE
SAS3
d
Aggregates size (μm²)
40
30
20
10
1.0
0.5
0.0
100
10
1
0.1
Dox concentration (μg/mL)

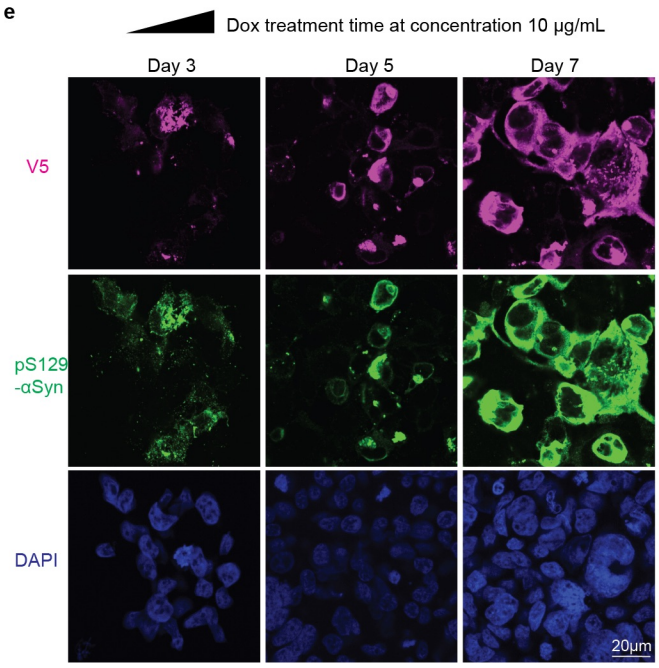
e
Dox treatment time at concentration 10 μg/mL
Day 3
Day 5
Day 7
V5
pS129
-αSyn
DAPI
20μm

Figure S1: Screening of SAS constructs in HEK cells and tunability of the SAS system.

a, Screening in HEK cells identifies SAS constructs that not only form αSyn aggregates but also induce substantial Ser129 phosphorylation of αSyn. **b,** Western blot of V5 tag and **c,** quantification show the expression level of SAS3 protein is lower than that induced by *SNCA* OE. n=3 biological replicates. **d,** Distribution of aggregate size induced by different dox concentrations. n=9 biological replicates. **e,** Immunostaining of V5 tag and pS129-αSyn after 3, 5, and 7 days of dox-induced SAS3 expression, demonstrating that aggregate size and level of pS129-aSyn increase with induction time. Scale bars equal 20 μm. Data are presented as mean ± SEM.

Figure S2

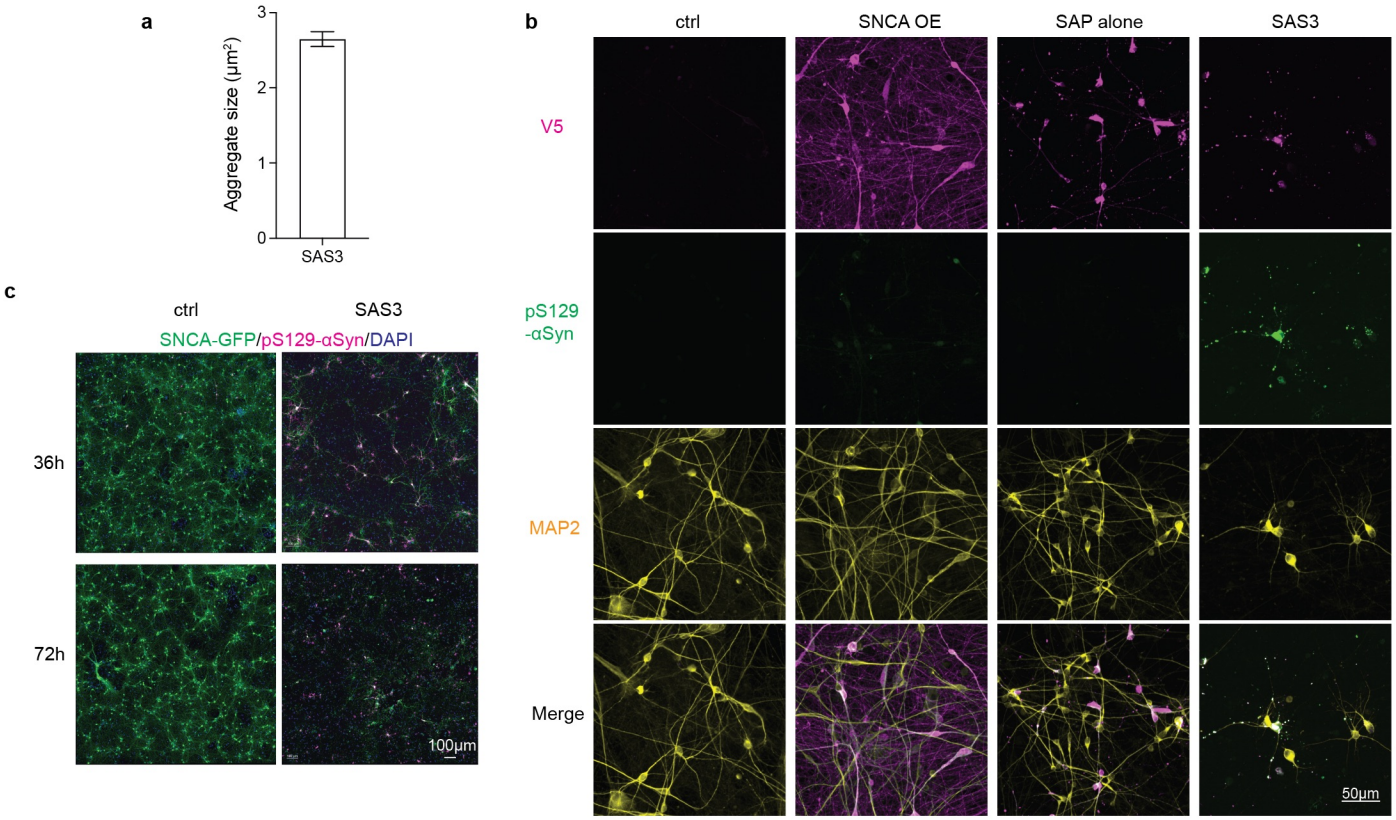
a
Aggregate size (μm²)
3
2
1
0
SAS3
b
ctrl
SNCA OE
SAP alone
SAS3
V5
pS129
-αSyn
MAP2
Merge
50μm
c
ctrl
SAS3
SNCA-GFP/pS129-αSyn/DAPI
36h
72h
100μm

Figure S2: SAS induces neurite retraction and endogenous αSyn aggregation in hESC-derived neurons.

a, Quantification of average aggregate size induced by SAS3 in mouse primary neurons. **b,** Immunostaining of V5 tag and pS129-αSyn in transduced hESC-derived human cortical neurons after 3 days of dox treatment shows that SAS3 induces αSyn aggregation, strong αSyn phosphorylation, and neurite retraction. (**c**), Immunostaining after 36 and 72 hours of dox treatment indicates that neurons expressing SAS3 display degeneration at 36 hours which further worsens by 72 hours. Data are presented as mean ± SEM.

Figure S3

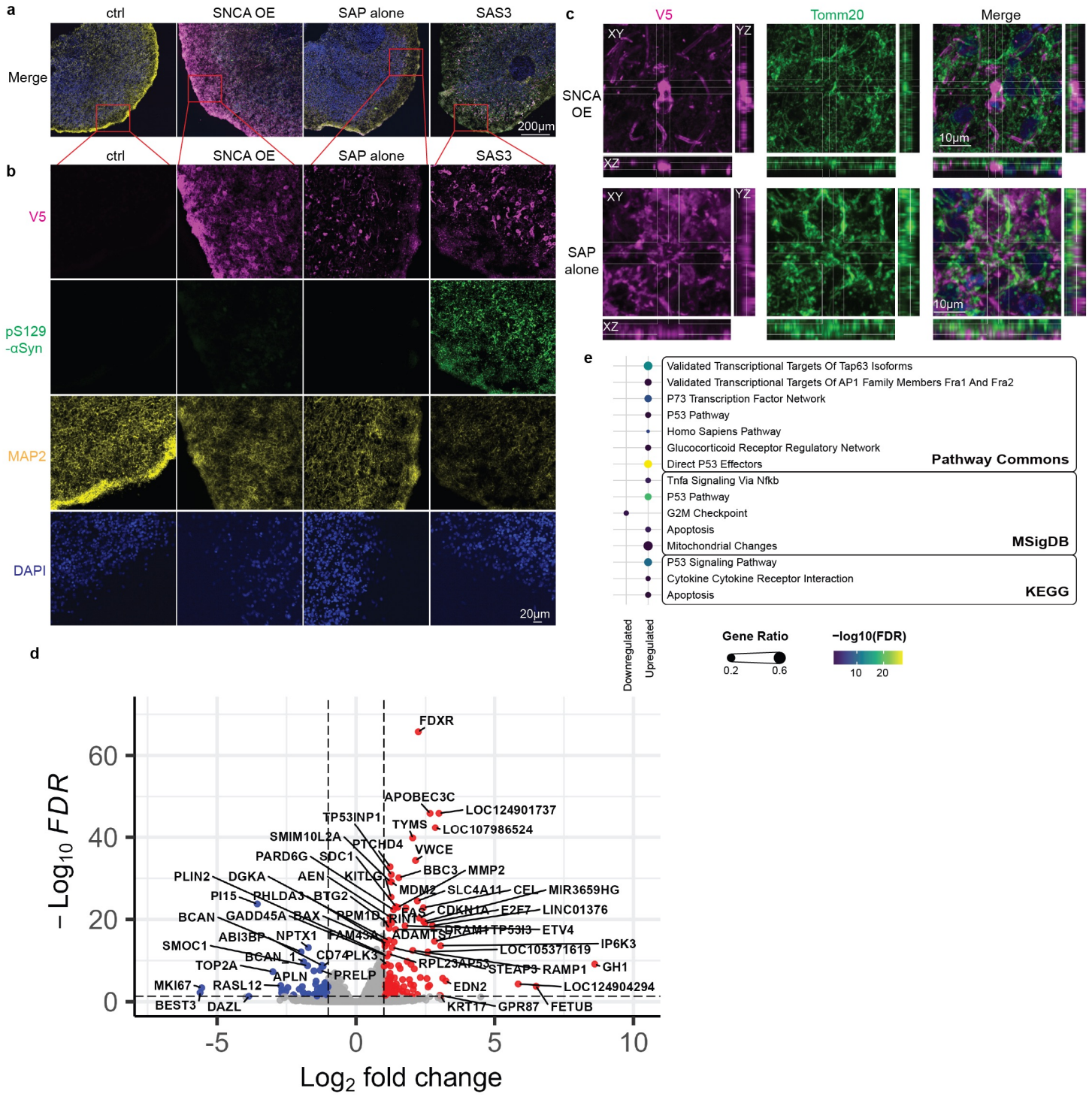
a
ctrl
SNCA OE
SAP alone
SAS3
Merge
200μm
b
V5
pS129 -αSyn
MAP2
DAPI
20μm
c
V5
Tomm20
Merge
SNCA OE
SAP alone
XY
YZ
XZ
10μm
e
Validated Transcriptional Targets Of Tap63 Isoforms
Validated Transcriptional Targets Of AP1 Family Members Fra1 And Fra2
P73 Transcription Factor Network
P53 Pathway
Homo Sapiens Pathway
Glucocorticoid Receptor Regulatory Network
Direct P53 Effectors
Pathway Commons
Tnfa Signaling Via Nfkb
P53 Pathway
G2M Checkpoint
Apoptosis
Mitochondrial Changes
MSigDB
P53 Signaling Pathway
Cytokine Cytokine Receptor Interaction
Apoptosis
KEGG
Downregulated
Upregulated
Gene Ratio
0.2
0.6
−log10(FDR)
10
20
d
FDXR
APOBEC3C
LOC124901737
TP53INP1
TYMS
LOC107986524
SMIM10L2A
PTCHD4
VWCE
PARD6G
SDC1
BBC3
MMP2
PLIN2
DGKA
AEN
KITLG
MDM2
SLC4A11
CEL
MIR3659HG
PI15
PHLDA3
BTG2
FAS
CDKN1A
E2F7
LINC01376
BCAN
GADD45A
BAX
PPM1D
RIN1
DRAM1
TP53I3
ETV4
ABI3BP
NPTX1
FAM43A
ADAMTS7
IP6K3
SMOC1
LOC105371619
BCAN
CD74
PLK3
TOP2A
RPL23AP53
STEAP3
RAMP1
GH1
APLN
PRELP
MKI67
RASL12
EDN2
LOC124904294
BEST3
DAZL
KRT17
GPR87
FETUB
$-\log_{10} FDR$
$\log_2$ fold change
60
40
20
0
-5
0
5
10

Figure S3: The genetically-encoded SAS system enables efficient access to organoids.

a-b, Immunostaining of V5 tag and pS129-αSyn in transduced human cortical organoids after 3 days of dox treatment. Compared to *SNCA* OE and SAP alone, only SAS3 induces αSyn aggregation, strong αSyn S129 phosphorylation, and neuron degeneration. Scale bar equals 200 μm and 20 μm in enlargement. **c,** Z-stack scanning of organoids stained for V5 tag and the mitochondrial marker Tomm20, showing that *SNCA* OE and SAP construct-produced proteins do not colocalize with mitochondria, shown by XY (main), XZ (bottom panel) and YZ (right panel) projections. Scale bars equal 10 μm. **d,** Volcano plot of transcriptomic data labeling all DEGs with FDR < 0.05 and log2 fold change (FC) >1. Genes upregulated in SAS-treated organoids are shown in red and downregulated in blue. **e,** Pathway analysis of DEGs using different databases reveals that SAS3-treated organoids are characterized by significant up-regulation of pathways associated with apoptosis, inflammation, and mitochondrial changes.

Figure S4

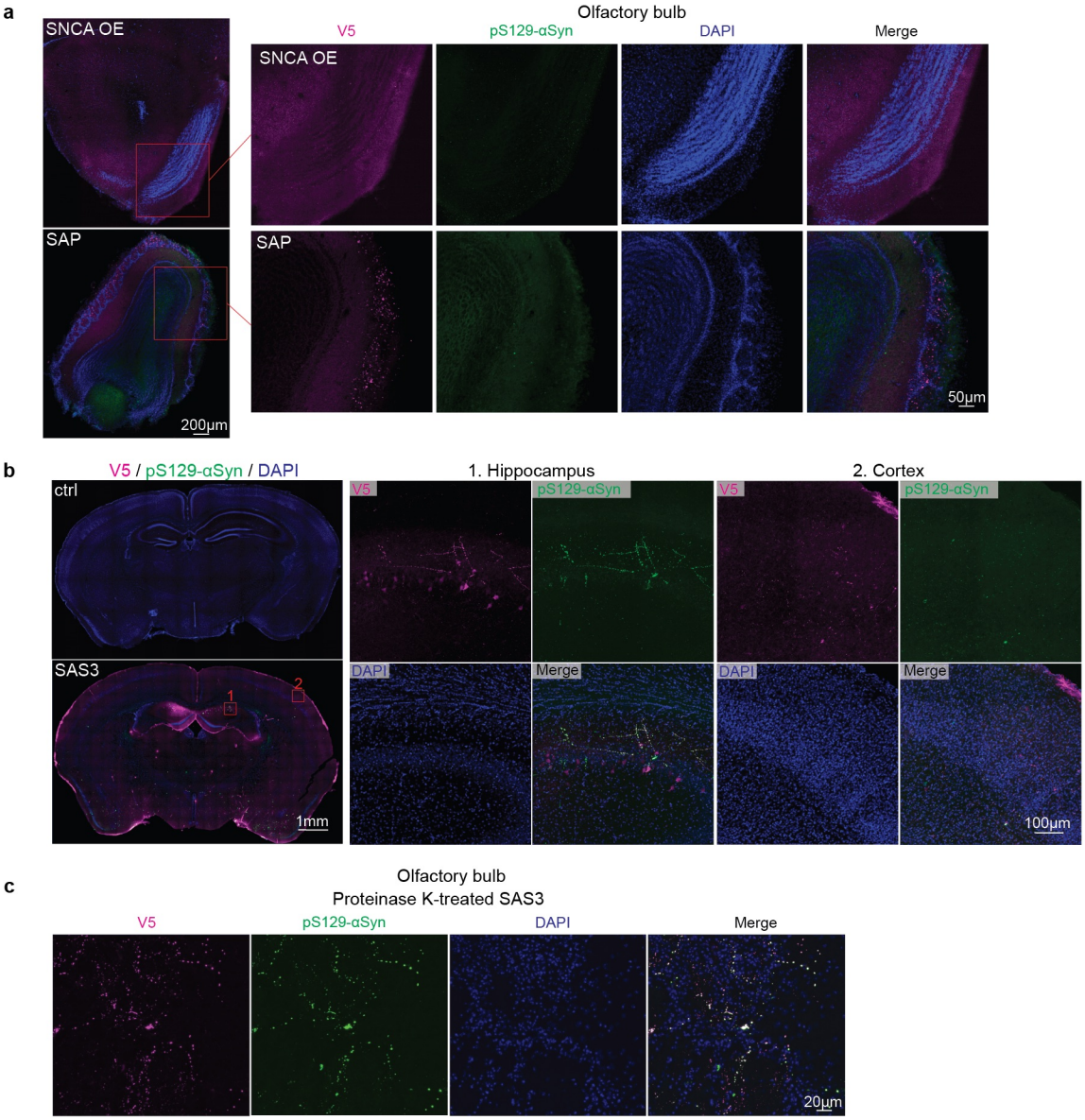
a
SNCA OE
SAP
200μm
Olfactory bulb
V5
pS129-αSyn
DAPI
Merge
SNCA OE
SAP
50μm
b
V5 / pS129-αSyn / DAPI
1. Hippocampus
2. Cortex
ctrl
SAS3
1
2
1mm
V5
pS129-αSyn
DAPI
Merge
100μm
c
Olfactory bulb
Proteinase K-treated SAS3
V5
pS129-αSyn
DAPI
Merge
20μm

Figure S4: SAS induces PD-relevant histopathology.

a, Immunostaining for the V5 tag and pS129-αSyn in the olfactory bulb of C57BL/6J mice, showing that *SNCA* OE and SAP-alone constructs do not induce strong αSyn phosphorylation in olfactory bulb. Scale bar equals 200 μm and 50 μm in enlargement. **b,** Immunostaining for the V5 tag and pS129-αSyn in the hippocampus and cortex of SAS3-treated or control mice, showing aggregates and strong αSyn phosphorylation in neurons induced by SAS3. Scale bar equals 1 mm and 100 μm in enlargement. **c,** Immunostaining for the V5 tag and pS129-αSyn in the olfactory bulb of SAS3-treated mice after proteinase K treatment, showing resistance of aggregates to degradation. Scale bar equals 20 μm.

Figure S5

a
ctrl
SAS3
GO.immune_response
GO.defense_response_to_virus
GO.inflammatory_response
GO.external_side_of_plasma_membrane
GO.innate_immune_response
GO.cytokine_mediated_signaling_pathway
GO.interferon_gamma_mediated_signaling_pathway
GO.signal_transduction
GO.negative_regulation_of_viral_genome_replication
GO.regulation_of_immune_response
GO.T_cell_costimulation
GO.type_I_interferon_signaling_pathway
GO.receptor_activity
GO.T_cell_activation
GO.T_cell_receptor_signaling_pathway
GO.antigen_processing_and_presentation_of_exogenous_peptide_antigen_via_MHC_class_I
GO.cellular_response_to_interferon_gamma
GO.neutrophil_chemotaxis
GO.cell_surface_receptor_signaling_pathway
GO.chemokine_mediated_signaling_pathway
GO.cellular_defense_response
GO.defense_response_to_protozoan
GO.positive_regulation_of_interferon_gamma_production
GO.positive_regulation_of_T_cell_proliferation
GO.plasma_membrane
GO.chemotaxis
GO.positive_regulation_of_tumor_necrosis_factor_production
GO.chemokine_activity
GO.B_cell_receptor_signaling_pathway
GO.cellular_response_to_lipopolysaccharide
GO.response_to_stimulus
down
up
Condition
-log10(FDR)
20
10
0
GeneRatio
0.1
0.2
0.3
0.4

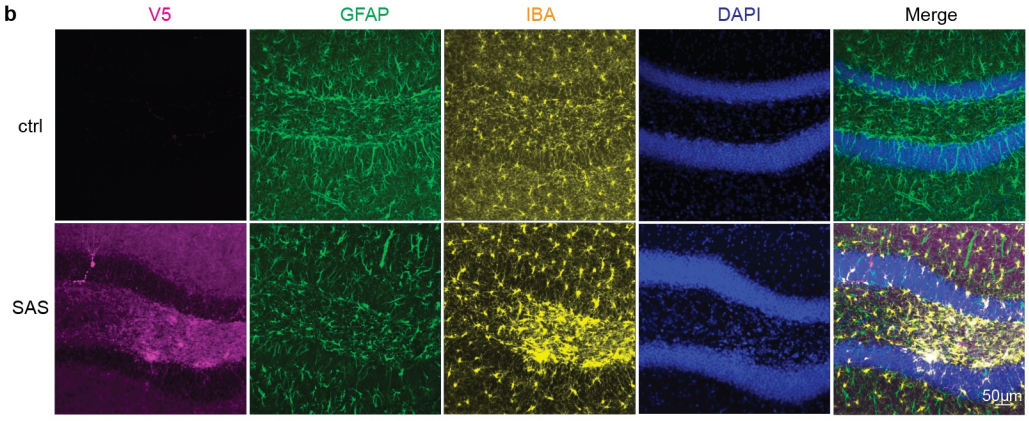
b
V5
GFAP
IBA
DAPI
Merge
ctrl
SAS
50μm

Figure S5: SAS actives microglia and triggers immune response in mice

a, All significantly differentially regulated GO pathways, revealing that SAS3-transduced mice show significant up-regulation of pathways associated with inflammation and immune response. **b,** Immunostaining for GFAP and IBA1 in the hippocampus, showing activated microglia clustered around SAS-induced aggregates. Scale bar equals 50 μm.

Figure S6

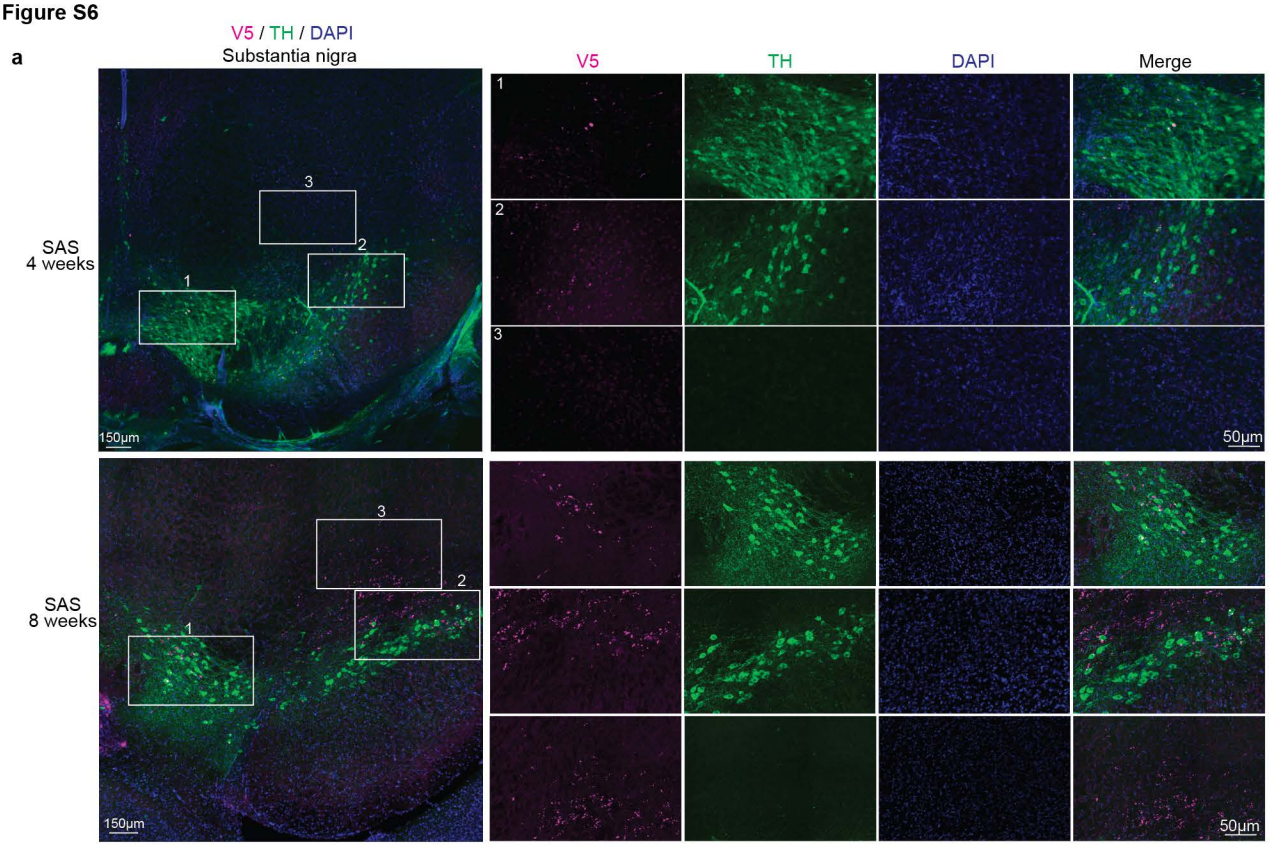
a
V5 / TH / DAPI
Substantia nigra
V5
TH
DAPI
Merge
SAS
4 weeks
SAS
8 weeks
1
2
3
150μm
50μm

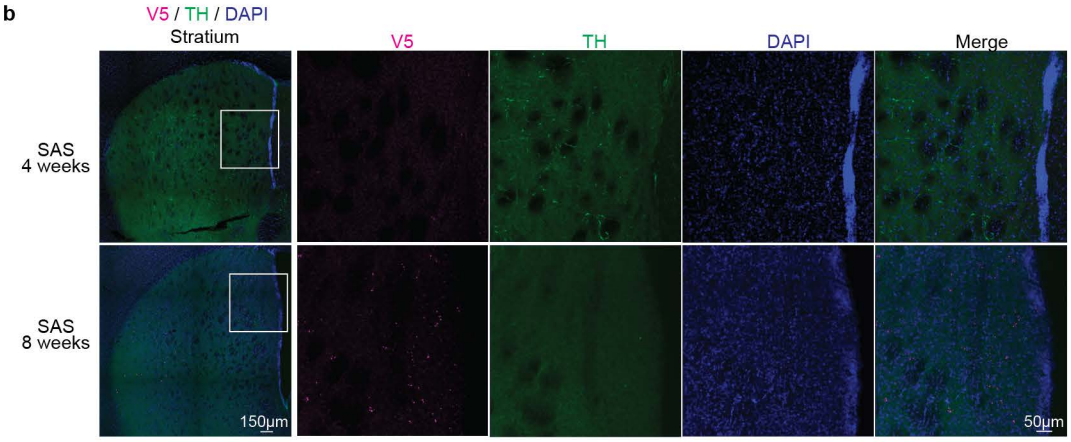
b
V5 / TH / DAPI
Stratium
V5
TH
DAPI
Merge
SAS
4 weeks
SAS
8 weeks
150μm
50μm

Figure S6: Dopaminergic neuron-targeted SAS recapitulates PD progression.

a, Immunostaining for the V5 tag and TH in the SN region of SAS3-treated TH-Cre mice with enlarged images of the ventral tegmental area (VTA, area 1), SNpc (area 2), and non-TH+ region (area 3). Scale bars equal 150 μm and 50 μm in enlargements. **b,** Immunostaining for the V5 tag and TH in the striatum, indicating progressive aggregate accumulation and potential spreading along the nigrostriatal pathway. Scale bar equals 150μm and 50 μm in enlargement.